Title:

Climate controls on fluvial topography

Authors:

Eyal Marder[1], Sean F. Gallen[1]

Affiliation:

[1]Department of Geosciences, Colorado State University, Fort Collins, Colorado 80523, USA

Corresponding author:

Eyal Marder, eyal.marder@colostate.edu

Climate controls on fluvial topography

Eyal Marder[1], Sean F. Gallen[1]

[1]Department of Geosciences, Colorado State University, Fort Collins, Colorado 80523, USA

Abstract

Conceptual and theoretical models for landscape evolution suggest that fluvial topography is sensitive to climate. However, it has remained challenging to demonstrate a compelling link between fluvial topography and climate state in natural landscapes. One possible reason is that many studies compare erosion rates to climate data, although theoretical studies note that, at steady-state, climate is encoded in topography rather than in erosion rates. Here, we use an existing global compilation of ^{10}Be basin average erosion rates to isolate the climate signal in topography for fluvially-dominated catchments underlain by crystalline bedrock that appear to be in morphological steady state. Our results show that the nonlinearity between erosion rates and the normalized river channel steepness index, which is a proxy for fluvial relief, systematically increases with increasing mean annual precipitation and decreasing aridity. When interpreted in the context of detachment-limited bedrock incision models that account for incision thresholds and stochastic distribution of floods, this systematic pattern can be explained by a decrease in discharge variability in landscapes that are wetter and less arid, assuming incision thresholds are important. Our results imply a climate control on topography at a global scale and highlight new research directions that can improve understanding of climate's impact on landscape evolution.

Introduction

Geologists and geomorphologists have long been motivated to understand the relationships between tectonics, climate, and landscape evolution (Molnar and England, 1990; Whipple et al., 1999; Willett, 1999). In the last decades, there has been a concerted effort by geomorphologists to characterize and quantify the impact of climate on landscape evolution in natural settings (e.g., Riebe et al., 2001; von Blanckenburg, 2005; Harel et al., 2016; Chen et al., 2019). Much of this work has focused on fluvially-dominated landscapes, where studies often compare long-term erosion rates from isotopic proxies (e.g., ^{10}Be) with measurable climate proxies (e.g., mean annual precipitation). Such comparisons typically show little-to-no correlation between climate and erosion rate, which is used to argue that climate is not a first-order driver of landscape dynamics (e.g., Riebe et al., 2001; von Blanckenburg, 2005). In contrast, studies that carefully selected transient river systems with strong precipitation gradients show clear correlations

between erosion rate or bulk erodibility and mean annual precipitation or precipitation variability (e.g., Moon et al., 2011; Ferrier et al., 2013; Gayer et al., 2019). Similarly, studies of morphologically steady-state bedrock rivers show that the functional relationship between fluvial topography and erosion rates systematically changes with precipitation, where all else being equal, basins that receive higher precipitation rates are less steep than basins that receive less rainfall (Adams et al., 2020).

These studies highlight two critical points. First, climate appears to have a measurable impact on landscape response time and bulk erodibility, such that for transient landscapes, basins that receive more precipitation will attain equilibrium faster and will have higher time-averaged erosion rates during landscape adjustment relative to basins that receive less precipitation (e.g., Ferrier et al., 2013). Second, at steady state, the climate signal is recorded in topography rather than in the long-term erosion rate because topography dynamically adjusts its geometry to erode and transport sediment at a rate equal to the tectonically or isostatically imposed rock uplift rate (Hack, 1960; Whipple et al., 1999; Adams et al., 2020). While such studies demonstrate that climate can impact landscapes at local-to-regional scales, no systematic global analysis has been conducted to determine if there is a climate signature encoded in landscape morphology globally.

Here, we fill this knowledge gap by conducting a global analysis of fluvially-dominated bedrock basins that appear to be morphologically in steady-state and that incise into similar crystalline rock types (Figs. 1, DR1, DR2). Leveraging an existing global compilation of cosmogenic ^{10}Be-derived erosion rates, a digital elevation model (DEM), global rock type, and global climate proxy data sets, we test for relationships between climate and landscape morphology (Figs. DR1, DR2; Table DR1). Through this analysis, we demonstrate a clear, systematic relationship between climate and topography that points to specific controlling mechanisms. We conclude by discussing the implications of these mechanisms in the context of climate, hydrology, and landscape evolution.

Materials and Methods

Tectonic geomorphology studies consistently demonstrate that in bedrock river systems, long-term erosion rate, E, and the normalized channel steepness, k_{sn}, defined as the local channel steepness normalized to its upstream drainage area, are empirically related via a power function (DiBiase et al., 2010; Kirby and Whipple, 2012; Lague, 2014; Harel et al., 2016):

$$E = C{k_{sn}}^{p} \quad (1),$$

where C and p are empirical constants. Numerous empirical studies and theoretical models for bedrock river incision that include incision thresholds and stochastic flood distributions, show that the relationship between E and k_{sn} is well described by equation 1 and largely controlled by hydroclimate (GSA Data Repository, herein GSA DR; Lague et al., 2005; DiBiase and Whipple, 2011; Lague, 2014; Deal et al., 2018).

Here we explore p in the context of changes in mean annual precipitation (MAP), aridity index (AI), mean annual temperature (MAT), and mean basin elevation (ME) (Fig. DR1). We use an existing standardized global compilation of basin average erosion rates derived from ^{10}Be concentrations in quartz-rich fluvial sands in fluvially-dominated basins (Figs. 1, DR1; Table DR1; Codilean et al., 2018). We derive the average k_{sn}, and a MAP-weighted version of this metric, $k_{sn}Q$ (Adams et al., 2020), for each of these basins, using a 3-arc second Shuttle Radar Topographic Mission (SRTM) DEM and a global MAP dataset (Fig. DR1; Table DR1; 'WorldClim 2'; Fick and Hijmans, 2017). We calculate k_{sn} from the slope of a linear regression through the river network elevation, z, and the transformed distance coordinate χ (known as χ-plots) for areas draining ≥ 1 km^2 (GSA DR; Fig. 1, inset; Perron et al., 2013) using a reference concavity index of 0.5, which is a common value for many river systems globally (GSA DR; Kirby and Whipple, 2012; Harel et al., 2016).

To best isolate the climate signal on fluvial topography, we attempt to control for rock type and uplift rate related changes in erodibility by restricting our analysis to bedrock rivers that drain ≥ 90% crystalline rocks ('GLiM'; Hartmann and Moosdorf, 2012; note distribution of plutonic and metamorphic units exhibit no systematic relationship with climate proxies; GSA DR; Fig. DR2; Table DR1) and basins that appear to be morphologically in steady-state with an R^2 ≥ 0.9 in χ-plots (Fig. 1, inset; although note we do not find results presented herein to be sensitive to changes in R^2; GSA DR; Table DR2). We also restrict our analysis to basins draining ≥ 10 km^2 to reduce potential biases in ^{10}Be concentrations imposed by land sliding (Yanites et al., 2009) and basins with MAP > 200 mm/yr to ensure that fluvial erosion is the dominant landscape denudation process.

For the remaining basins, we calculate the average values for MAP, MAT ('WorldClim 2'; Fick and Hijmans, 2017), AI ('CGIAR-CSI'; Trabucco and Zomer, 2009), and ME (SRTM DEM) (Table DR1). We bin the $E - k_{sn}$ and $E - k_{sn}Q$ data by increments of each respective climate variable, ensuring an equal number of data points in each bin, with minimum of 15 data points per bin (Fig. DR3). We calculate p and C for each climate bin using total least-square linear regressions through the log-transformed $E - k_{sn}$ and $E - k_{sn}Q$ data (Fig. DR4). In a separate analysis, we attempt to account for the general nonlinearity in the global dataset by conducting normalized regressions using a fixed p of 2.2 based on a regression through the entire

dataset, to calculate the normalized y-intercept, C_{ne}, for each climate bin (Fig. DR5; GSA DR; Harel et al., 2016; Adams et al., 2020). For each regression in these analyses, we estimate goodness-of-fit by calculating the R^2, χ^2, and Kolmogorov-Smirnov two-sided p-value test at the 90% significance level for each regression (Figs. DR3, DR5; Table DR2). We conduct several sensitivity analyses to evaluate the robustness of signals in p with changes in climate proxies by changing the number of bins for each climate variable and changing the R^2 threshold used to define morphological steady-state (GSA DR; Fig. DR6). For each of these tests, we estimate the same goodness-of-fit metrics described above (Table DR2).

Climate control on E-k_{sn} nonlinearity

Our results show systematic changes in the functional relationship between E and k_{sn} or $k_{sn}Q$ with changes in MAP and AI (Figs. 2, DR3). Because C and p in equation 1 covary, we focus on the exponent, p, which determines the degree of nonlinearity in the $E - k_{sn}$ and $E - k_{sn}Q$ relationships. We find that p systematically increases with increasing MAP (i.e., wetter) and AI (i.e., more humid) values (Figs. 3, DR4; Table DR2). For an increase in MAP from 500 to 4000 mm/yr and an increase of AI from 0.25 to 2, p increases from ~1.5-2 to ~3.5-4, with a slightly higher goodness-of-fit for AI (Figs. 3, DR4; Table DR2). We note that regressions for the highest MAP (>1717 mm/yr) and AI (>2) bins fit the data poorly (Figs. 2, DR3, DR6; Table DR2). These poor fits are likely due to the high chemical weathering in extremely wet and humid settings, which bias the typical relationship between denudation rates and ^{10}Be concentrations, making standard calculations of basin average erosion rate from ^{10}Be concentrations unreliable (e.g., Riebe and Granger, 2013). Excluding these high MAP and AI values, all other fits, which span most of the range of global climate conditions, show statistically significant relationships between E and k_{sn} with systematic changes in MAP and AI (Figs. 2, DR3, DR6; Table DR2). We do not find significant fits and systematic changes in p with ME and MAT (Figs. DR3, DR4, DR6; Table DR2). Under a fixed p of 2.2, C_{ne} generally decreases from ~10^{-8}m^{-7}yr^{-1} to ~10^{-9}m^{-8}yr^{-1} with increasing MAP and AI, but have poor fits, suggesting that variations in the degree of nonlinearity is critical to explain the data (Fig. DR5; Table DR2). Importantly, p values derived from E - $k_{sn}Q$ data show similar climate sensitivity as E - k_{sn}, implying that the incorporation of precipitation patterns do not explain systematic variations in fluvial topography with climate at the global scale (Figs. 3, DR3, DR5; cf. Adams et al., 2020). For both $E - k_{sn}$ and $E - k_{sn}Q$, sensitivity analyses show that systematic changes in p as a function of changes in MAP and AI are statistically robust to the number of climate bins used to segregate data and the R^2 threshold used to define morphologically steady-state basins (Figs. 3, DR6; Table DR2).

Interpretation of climate control on fluvial topography

Our results demonstrate a clear climate signal in topographic form based on systematic variations in the degree of nonlinearity of $E - k_{sn}$ (i.e., changing p) as a function of MAP and AI (Figs. 2, 3, DR3, DR6). We interpret these findings in the context of simple models for detachment-limited bedrock channel incision that account for stochastic flood distributions and incision thresholds (herein STIMs; GSA DR). STIMs predict systematic changes in the degree of nonlinearity in $E - k_{sn}$ as a function of flood distributions when incision thresholds are significant (GSA DR; Lague et al., 2005; Lague, 2014; Deal et al., 2018). For instance, in threshold-dominated bedrock channels, the nonlinearity between E and k_{sn} will systematically decline with increasing discharge variability (Lague et al., 2005; DiBiase and Whipple, 2011). Further, empirical studies and simple soil-layer hydrology models show that discharge variability decreases with higher mean annual precipitation and lower aridity (GSA DR; Molnar et al., 2006; Lague, 2014; Deal et al., 2018). Thus, in bedrock channels where incision thresholds are relevant, the nonlinearity between E and k_{sn} is expected to increase with higher mean annual precipitation and decreasing aridity, which is precisely what our result show (Figs. 2, DR3).

The dependency of the degree of nonlinearity between E and k_{sn} (i.e., p) on discharge variability can be visualized using STIMs as a function of the normalized incision threshold (defined as the ratio of incision threshold to erosion rate, ψ/E) and discharge variability (GSA DR; Fig. 4A; Lague et al., 2005). In this model, discharge variability is approximated with an inverse gamma distribution via a shape parameter, k, where low to high k represents high to low variability (GSA DR; Lague et al., 2005). By comparing predicted k and p values from STIMs under locally-calibrated parameters (DiBiase and Whipple, 2011; Lague, 2014) with empirically determined k and p values from discharge daily records near some of our analyzed basins, we find that in both cases, k increases from ~0.1 to 3, and p increases from ~1 to 5 with increasing MAP and AI, consistent with both our global analysis and previous studies (GSA DR; Figs. 3, 4, DR7; Molnar et al., 2006; Lague, 2014; Deal et al., 2018). Thus, assuming STIMs are representative for the analyzed basins in this study, our results imply that incision thresholds are important, and that discharge variability decreases with increasing MAP and AI globally.

While, generally, STIMs provide a simple framework to explain our results, some nuances in our analysis are still not fully resolved. For example, p calculated for $E - k_{sn}Q$ and, C_{ne}, which attempt to control for some of the climate influence, show systematic variations with climate proxies (Figs. DR3, DR5). This finding suggests that climate-related variables studied and invoked here cannot fully account for observed variations in topography, and that other factors, such as the magnitude of incision threshold, grain

size distribution, channel width scaling, and dominant incision process, likely covary with the climate regime. Future efforts to understand the relationships between climate and landscape evolution in fluvially-dominated systems will ultimately reveal other dominant channel incision mechanisms that are most sensitive to climate. Despite some lingering questions, our results demonstrate a clear and systematic change in the degree of nonlinearity between E and k_{sn} or $k_{sn}Q$ as a function of MAP and AI, providing compelling evidence for a correlation between landscape morphology and climate on a global scale (Figs. 2, 3, DR3, DR6).

Acknowledgments

The authors thank Colorado State University for partial financial support of this research.

References

Adams, B.A., Whipple, K.X., Forte, A.M., Heimsath, A.M., and Hodges, K.V., 2020, Climate controls on erosion in tectonically active landscapes: Science Advances, v. 6, p. eaaz3166, doi:10.1126/sciadv.aaz3166.

von Blanckenburg, F., 2005, The control mechanisms of erosion and weathering at basin scale from cosmogenic nuclides in river sediment: Earth and Planetary Science Letters, v. 237, p. 462–479, doi:10.1016/j.epsl.2005.06.030.

Chen, S.-A., Michaelides, K., Grieve, S.W.D., and Singer, M.B., 2019, Aridity is expressed in river topography globally: Nature, v. 573, p. 573–577, doi:10.1038/s41586-019-1558-8.

Codilean, A.T., Munack, H., Cohen, T.J., Saktura, W.M., Gray, A., and Mudd, S.M., 2018, OCTOPUS: an open cosmogenic isotope and luminescence database: Earth System Science Data, v. 10, p. 2123–2139, doi:10.5194/essd-10-2123-2018.

Deal, E., Braun, J., and Botter, G., 2018, Understanding the Role of Rainfall and Hydrology in Determining Fluvial Erosion Efficiency: Journal of Geophysical Research: Earth Surface, v. 123, p. 744–778, doi:10.1002/2017JF004393.

DiBiase, R.A., and Whipple, K.X., 2011, The influence of erosion thresholds and runoff variability on the relationships among topography, climate, and erosion rate: Journal of Geophysical Research, v. 116, p. F04036, doi:10.1029/2011JF002095.

DiBiase, R.A., Whipple, K.X., Heimsath, A.M., and Ouimet, W.B., 2010, Landscape form and millennial erosion rates in the San Gabriel Mountains, CA: Earth and Planetary Science Letters, v. 289, p. 134–144, doi:10.1016/j.epsl.2009.10.036.

Ferrier, K.L., Huppert, K.L., and Perron, J.T., 2013, Climatic control of bedrock river incision: Nature, v. 496, p. 206–209, doi:10.1038/nature11982.

Fick, S.E., and Hijmans, R.J., 2017, WorldClim 2: new 1-km spatial resolution climate surfaces for global land areas: International Journal of Climatology, v. 37, p. 4302–4315, doi:10.1002/joc.5086.

Gayer, E., Michon, L., Louvat, P., and Gaillardet, J., 2019, Storm-induced precipitation variability control of long-term erosion: Earth and Planetary Science Letters, v. 517, p. 61–70, doi:10.1016/j.epsl.2019.04.003.

Hack, J.T., 1960, Interpretation of erosional topography in humid temperate regions: American Journal of Science, v. 258-A, p. 80–97.

Harel, M.-A., Mudd, S.M., and Attal, M., 2016, Global analysis of the stream power law parameters based on worldwide 10 Be denudation rates: Geomorphology, v. 268, p. 184–196, doi:10.1016/j.geomorph.2016.05.035.

Hartmann, J., and Moosdorf, N., 2012, The new global lithological map database GLiM: A representation of rock properties at the Earth surface: Geochemistry, Geophysics, Geosystems, v. 13, doi:10.1029/2012GC004370.

Kirby, E., and Whipple, K.X., 2012, Expression of active tectonics in erosional landscapes: Journal of Structural Geology, v. 44, p. 54–75, doi:10.1016/j.jsg.2012.07.009.

Lague, D., 2014, The stream power river incision model: evidence, theory and beyond: Earth Surface Processes and Landforms, v. 39, p. 38–61, doi:10.1002/esp.3462.

Lague, D., Hovius, N., and Davy, P., 2005, Discharge, discharge variability, and the bedrock channel profile: Journal of Geophysical Research: Earth Surface, v. 110, p. n/a-n/a, doi:10.1029/2004JF000259.

Molnar, P., Anderson, R.S., Kier, G., and Rose, J., 2006, Relationships among probability distributions of stream discharges in floods, climate, bed load transport, and river incision: Journal of Geophysical Research, v. 111, p. F02001, doi:10.1029/2005JF000310.

Molnar, P., and England, P., 1990, Late Cenozoic uplift of mountain ranges and global climate change: Chicken or egg? Nature, v. 346, p. 29–34, doi:10.1038/346029a0.

Moon, S., Page Chamberlain, C., Blisniuk, K., Levine, N., Rood, D.H., and Hilley, G.E., 2011, Climatic control of denudation in the deglaciated landscape of the Washington Cascades: Nature Geoscience, v. 4, p. 469–473, doi:10.1038/ngeo1159.

Perron, J.T., Royden, L., Niemi, N.A., Schildgen, T.F., Van Der Beek, P.A., Sinclair, H.D., and Thiede, R.C., 2013, An integral approach to bedrock river profile analysis: Earth Surface Processes and Landforms, v. 38, p. 570–576, doi:10.1002/esp.3302.

Riebe, C.S., and Granger, D.E., 2013, Quantifying effects of deep and near-surface chemical erosion on cosmogenic nuclides in soils, saprolite, and sediment: Earth Surface Processes and Landforms, v. 38, p. 523–533, doi:10.1002/esp.3339.

Riebe, C.S., Kirchner, J.W., Granger, D.E., and Finkel, R.C., 2001, Strong tectonic and weak climatic control of long-term chemical weathering rates: Geology, v. 29, p. 511, doi:10.1130/0091-7613(2001)029<0511:STAWCC>2.0.CO;2.

Trabucco, A., and Zomer, R.J., 2009, Global aridity index (global-aridity) and global potential evapo-transpiration (global-PET) geospatial database.: CGIAR Consortium for Spatial Information, v. 89, p. 1–2.

Whipple, K.X., Kirby, E., and Brocklehurst, S.H., 1999, Geomorphic limits to climate-induced increases in topographic relief: Nature, v. 401, p. 39–43, doi:10.1038/43375.

Willett, S.D., 1999, Orogeny and orography: The effects of erosion on the structure of mountain belts: Journal of Geophysical Research: Solid Earth, v. 104, p. 28957–28981, doi:10.1029/1999JB900248.

Yanites, B.J., Tucker, G.E., and Anderson, R.S., 2009, Numerical and analytical models of cosmogenic radionuclide dynamics in landslide-dominated drainage basins: Journal of Geophysical Research, v. 114, p. F01007, doi:10.1029/2008JF001088.

Figure Captions

Figure 1: (A) (Inset) k_{sn} calculation from river profiles in χ-z space in a steady-state basin in Japan (black square in A); we use a similar method to calculate $k_{sn}Q$ (see GSA Data repository; Fig. DR3). **(Main)** Global mean annual precipitation map (Fick and Hijmans, 2017) with locations of the analyzed steady-state basins with existing basin average erosion rates from the Octopus archive (Codilean et al., 2018). Also marked are the locations of stream gauge stations in Figures 4 and DR7. IDH = Idaho, USA; DEN = Denver, USA; App = Appalachians, USA; SGM = San Gabriel Mountains, USA; BRA = Florianopolis, Brazil; ALPS = European Alps; SAF = South Africa; MAD = Madagascar; SIND = Southwest India; TAW = Taiwan; JAP = Japan. **(B)** Global aridity index map (Trabucco and Zomer, 2009) with similar annotations as in (A).

Figure 2: Modeled regressions for k_{sn} versus E (equation 1) for 265 basins under a steady-state threshold of R^2 > 0.9 (Figure 1, inset; Figure DR6; Table DR1), where each data point represents one basin and is classified by its mean annual precipitation **(A)** and aridity index **(B)**. Noted are power law modeled regressions and their R^2 goodness-of-fit. For each climate bin, p and C are noted. For the highest MAP and AI climate bins, where goodness-of-fit is poor, regressions and data points are transparent and colored in grey. For full analysis, see Figure DR3 and Table DR2.

Figure 3: p values for modeled regressions in Figure 2 with changes in **(A)** MAP and **(B)** AI. Inset figures show p values under different number of climate bins (for full analysis of p with changes in climate proxies, number of bins, and different R^2 thresholds, see Figures DR4, DR6; Table DR2). Note a systematic increase in p with increased MAP (i.e., wetter) and AI (i.e., higher humidity). $k_{sn}Q$ does not significantly change values or systematic patterns in p. p values from poor fits are transparent (Table DR2).

Figure 4: (A) Modeled changes in p in equation 1 as a function of changes in the normalized threshold for channel incision, ψ/E. **(B)** Exceedance probability plots of mean daily discharge (m^3/s) recorded data in gauge stations near SGM, APP, and BRA (see locations in Figure 1). Mentioned are MAP, AI, and calculated k for basins near the gauge stations (GSA DR; Fig. DR7). The range and systematic increase in p from ~1.8 to 4 with increasing MAP and AI correspond with theoretical predictions of increase of p from ~1.8 to 4.5 under a threshold dominated regime (Lague, 2014), where in both cases, k increases from ~0.25 to 3.

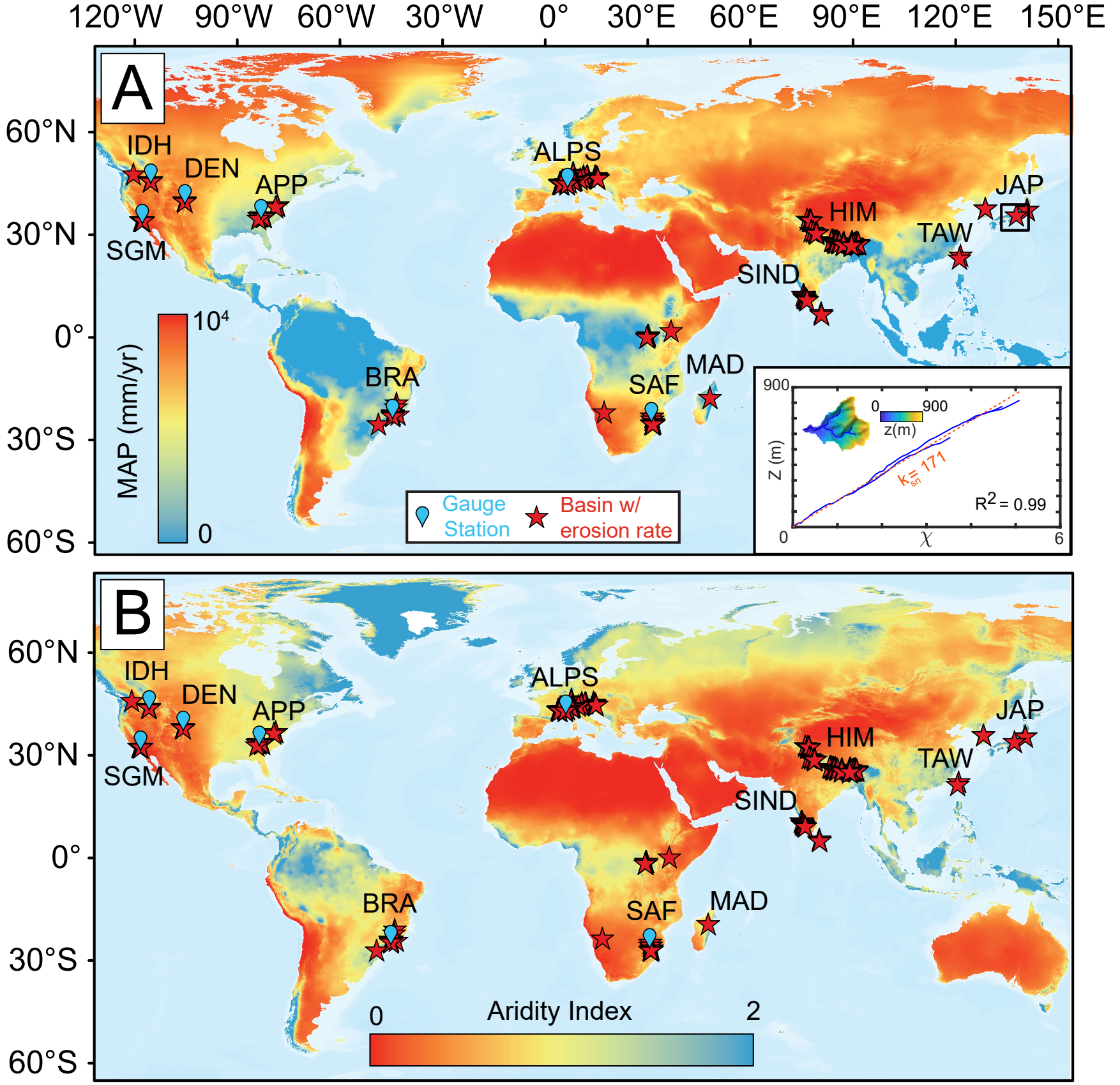
120°W
90°W
60°W
30°W
0°
30°E
60°E
90°E
120°E
150°E
A
60°N
30°N
0°
30°S
60°S
IDH
DEN
APP
SGM
ALPS
JAP
HIM
TAW
SIND
MAD
SAF
BRA
MAP (mm/yr)
10⁴
0
Gauge Station
Basin w/ erosion rate
900
0
z(m)
900
Z (m)
k_sn = 171
R² = 0.99
χ
0
6
B
60°N
30°N
0°
30°S
60°S
IDH
DEN
APP
SGM
ALPS
JAP
HIM
TAW
SIND
MAD
SAF
BRA
0
Aridity Index
2

Figure 1

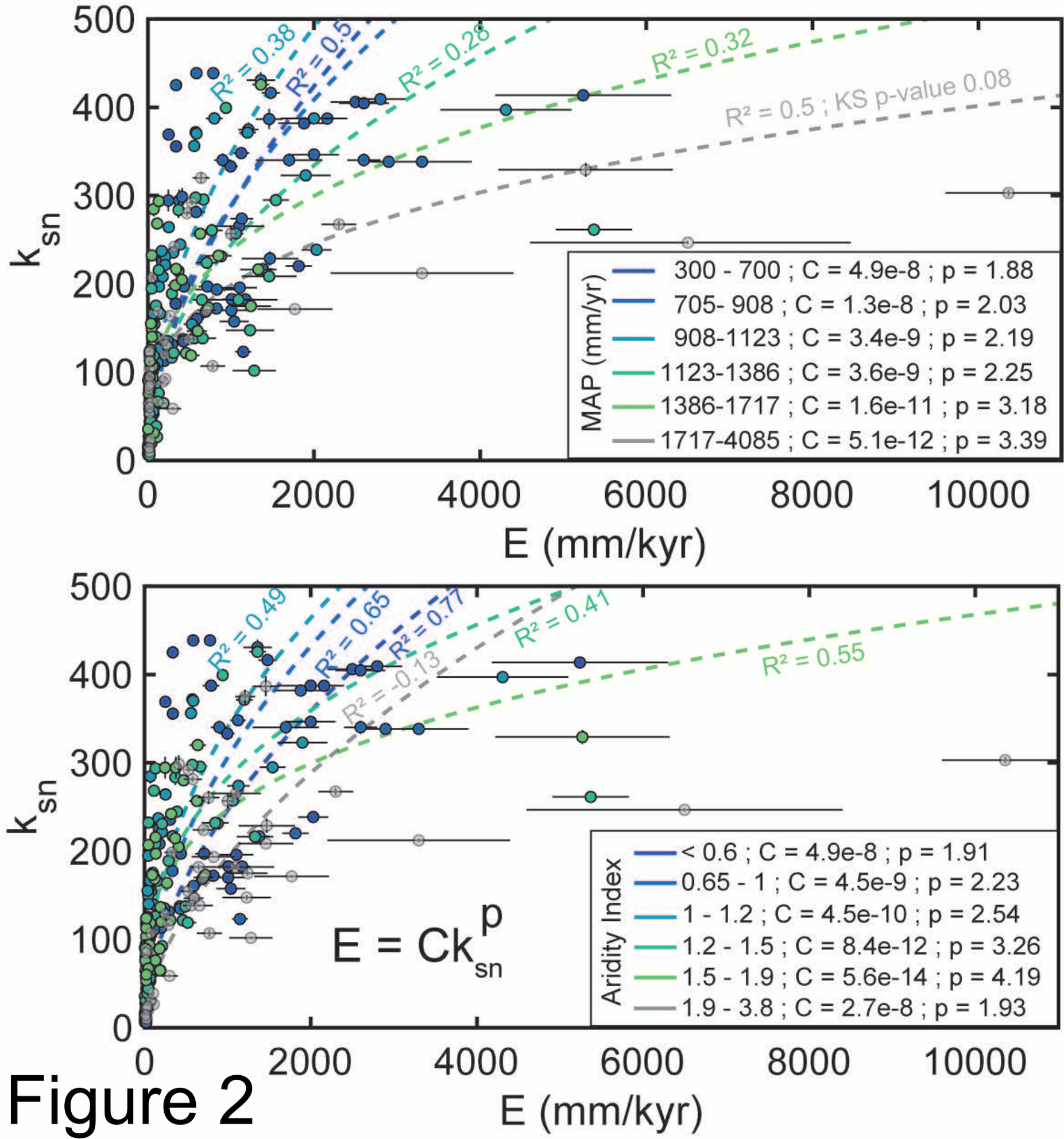
500
400
300
200
100
0
k_{sn}
0
2000
4000
6000
8000
10000
E (mm/kyr)
R^2 = 0.38
R^2 = 0.5
R^2 = 0.28
R^2 = 0.32
R^2 = 0.5 ; KS p-value 0.08
MAP (mm/yr)
300 - 700 ; C = 4.9e-8 ; p = 1.88
705- 908 ; C = 1.3e-8 ; p = 2.03
908-1123 ; C = 3.4e-9 ; p = 2.19
1123-1386 ; C = 3.6e-9 ; p = 2.25
1386-1717 ; C = 1.6e-11 ; p = 3.18
1717-4085 ; C = 5.1e-12 ; p = 3.39
R^2 = 0.49
R^2 = 0.65
R^2 = 0.77
R^2 = -0.13
R^2 = 0.41
R^2 = 0.55
$E = Ck_{sn}^{p}$
Aridity Index
< 0.6 ; C = 4.9e-8 ; p = 1.91
0.65 - 1 ; C = 4.5e-9 ; p = 2.23
1 - 1.2 ; C = 4.5e-10 ; p = 2.54
1.2 - 1.5 ; C = 8.4e-12 ; p = 3.26
1.5 - 1.9 ; C = 5.6e-14 ; p = 4.19
1.9 - 3.8 ; C = 2.7e-8 ; p = 1.93

Figure 2

Figure 3

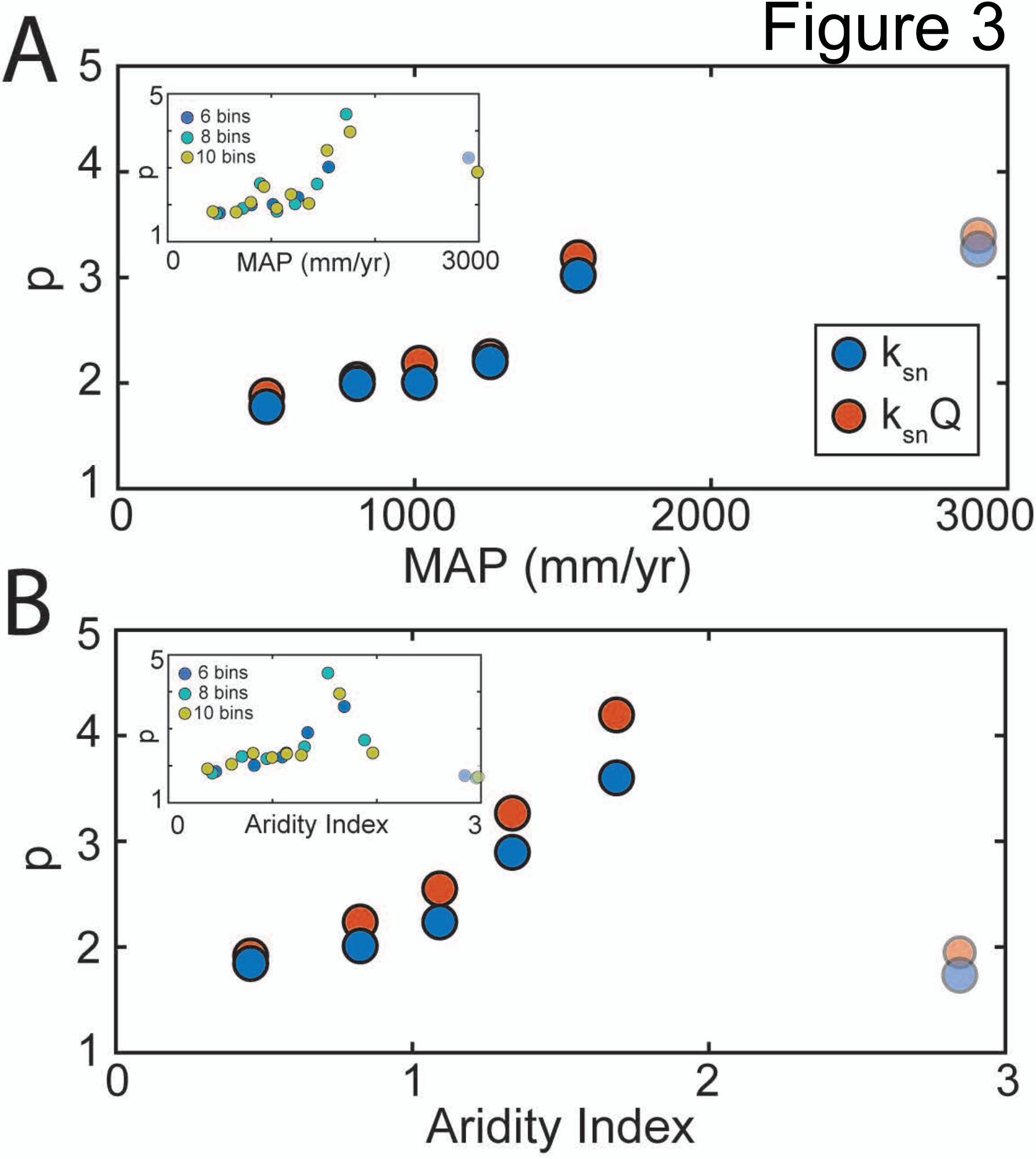

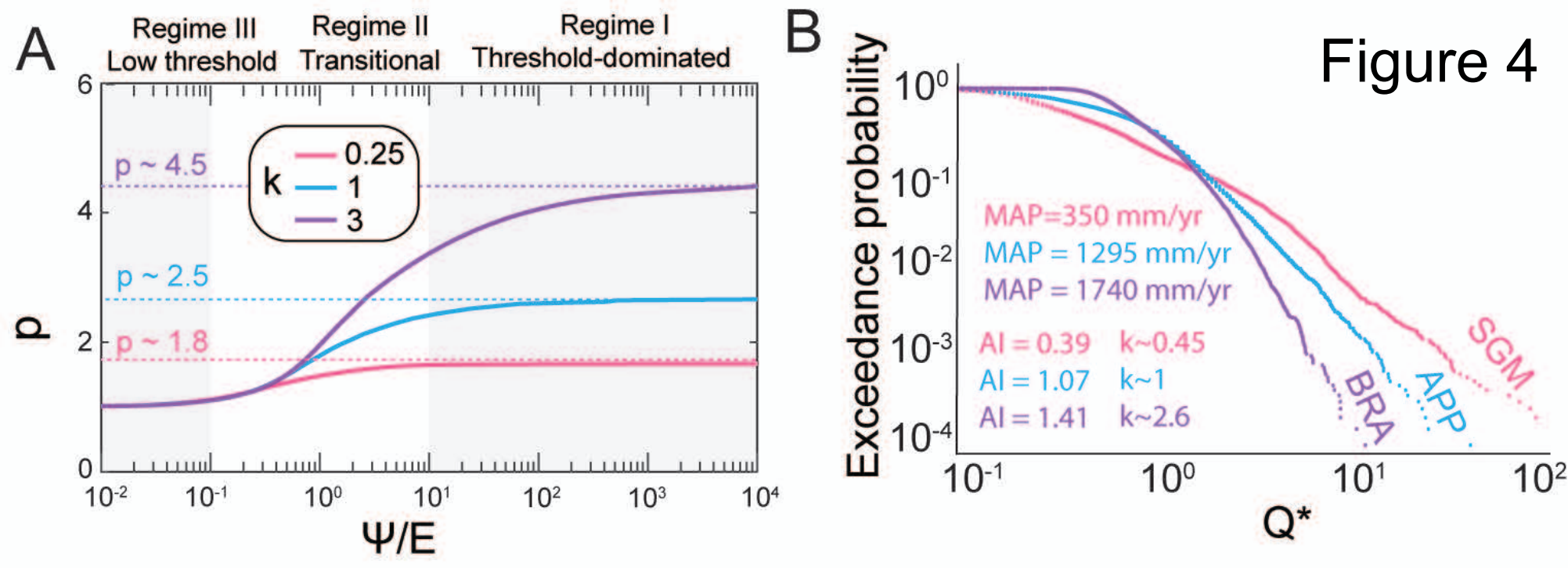
A
Regime III
Low threshold
Regime II
Transitional
Regime I
Threshold-dominated
p ~ 4.5
p ~ 2.5
p ~ 1.8
k
0.25
1
3
p
Ψ/E
B
Exceedance probability
MAP=350 mm/yr
MAP = 1295 mm/yr
MAP = 1740 mm/yr
AI = 0.39 k~0.45
AI = 1.07 k~1
AI = 1.41 k~2.6
SGM
APP
BRA
Q*

Figure 4

Supplementary Materials

- Text DR1
- Figure and table captions
- Figures DR1 to DR7
- Tables DR1, DR2

Text DR1

River profile analysis

For graded, steady-state river profiles, where the rock uplift rate, U, is balanced by the long term erosion rate, E, the relationship between local channel slope, S, and the upstream drainage area, A, can be described by a power function (Flint, 1974):

$$S = k_s A^{-\theta} \quad \text{(DR1)},$$

where k_s is the channel steepness index and θ is the channel concavity index (Kirby and Whipple, 2012). The covariation of k_s and θ requires normalization which is typically done by fixing θ to a reference value (i.e., reference concavity index, θ_{ref}) of ~0.3-0.7 to calculate the normalized channel steepness index k_{sn} (Kirby and Whipple, 2012; Lague, 2014; Harel et al., 2016). Equation DR1 can be used to derive k_s or k_{sn} empirically from regression through S and A data. However, such calculation introduces noise and requires a large amount of smoothing (Snyder et al., 2000; Wobus et al., 2006). Thus, it is preferable to use χ, a path-dependent integral parameter of the inverse of A raised to θ_{ref} (Royden and Perron, 2013):

$$\chi = \int_{x_b}^{x} \left(\frac{A_0}{A(x')}\right)^{\theta_{ref}} dx' \quad \text{(DR2)},$$

where x_b is the referenced distance at the drainage network outlet, x is the upstream distance along the channel, and A_0 is the referenced upstream drainage area, usually chosen as unity ($A_0 = 1$). Equation DR1, where $S = dz/dx$, can be integrated with respect to distance to generate a χ-elevation plot (typically referred to as a χ-plot):

$$z(x) = z(x_b) + k_{sn}\chi \quad \text{(DR3)},$$

where the slope of a linear regression of $\chi - z$ is k_{sn}. We calculate χ by implementing A and drainage area weighted by the spatial distribution of mean annual precipitation, $MAP \times A$, in equation DR2, using ChiProfiler (Gallen and Wegmann, 2017). We use χ and the precipitation-weighted χ to calculate k_{sn} and

$k_{sn}Q$ (cf. Adams et al., 2020), respectively, by calculating linear regressions through the basin-wide χ-z data (Equation DR3; Fig. 1, inset in the main text). We calculate the R^2 for each of these linear regressions to determine the basin morphological steady state, where higher R^2 values reflect basins that appear to be morphologically in steady state (i.e., roughly linear χ-z plots), and low R^2 values reflect basins that are in transient state (Fig. 1, inset in the main text). We conduct this analysis for all basins with published ^{10}Be cosmogenic nuclide basin average erosion rates from fluvial sands from the Octopus archive (Codilean et al., 2018).

Binning, regressions, and sensitivity analyses

We use existing global climate data of mean annual precipitation (MAP), mean annual temperature (MAT) (Fick and Hijmans, 2017), aridity index (AI) (Trabucco and Zomer, 2009), and SRTM 3-arc second digital elevation model (DEM) tiles (ME) (OpenTopography) to calculate mean climate proxy values for each basin (Figs. 1 in the main text, DR1; Table DR1). We convert all global data to rasters, project them to the WGS 84 geographic coordinate system, and crop them to the basin geometries, using Arc Pro 2.0.8. We project the basin rasters to a UTM coordinate system, resample them to 90 m cell size, calculate their mean MAP, MAT, AI, and ME values using Matlab and TopoToolbox (Schwanghart and Scherler, 2014), and compile this data with E, k_{sn}, and $k_{sn}Q$ data for each basin (Table DR1). To control for bedrock variability, we restrict our analysis to bedrock rivers that drain ≥ 90% crystalline rocks (plutonic and metamorphic units) based on a global composite geological map (Fig. DR2A; 'GLiM'; Hartmann and Moosdorf, 2012). We calculate the distribution and dominance of plutonic and metamorphic units and compare them to MAP, MAT, AI, and ME in each basin to ensure that there is no global relationship between rock type and climate variability (Fig. DR2B; Table DR1).

We bin the $E - k_{sn}$ and $E - k_{sn}Q$ datasets based on increments of MAP, MAT, AI, and ME (Fig. DR3). We select the bins to have an equal number of data points, with at least 15 data points in each bin. For each climate bin, we conduct a linear regression through log-transformed $E - k_{sn}$ and $E - k_{sn}Q$ data using total least squares to determine the power-law exponent, p, and its constant, C, in equation 1 (main text) (Fig. DR4). We assess the relationships between these parameters and the climate proxy data to evaluate if systematic patterns exist (Fig. DR4). We attempt to account for the general nonlinearity (i.e., p) in the global dataset by conducting normalized regressions through the data under a fixed p~2.2 (i.e., the global value of our dataset; cf. Harel et al., 2016; Adams et al., 2020) to determine the normalized y-intercept, C_{ne}, for the $E - k_{sn}$ and $E - k_{sn}Q$ data sets (Fig. DR5; Table DR2). For all modeled regressions,

we calculate the statistical goodness-of-fit metrics of R^2, χ^2, and Kolmogorov-Smirnov two-sided p-value at the 90% significance level to evaluate the significance of p and C_{ne} in our analysis (Table DR2).

We conduct several sensitivity analyses to evaluate the robustness of p in our modeled regressions, namely testing the impact of the number of bins with equal number of data points per bin (e.g., for the dataset in Table DR1, 4 bins with 66 points per bin, 6 bins with 44 points per bin, 8 bins with 33 points per bin, etc.; Fig. DR6A) and testing for the impact of transience in our basin analysis by changing the minimum R^2 morphological threshold value from $R^2 = 0.75$ to $R^2 = 0.95$ (Figs. 1, inset in main text, DR6B; Table DR2). Generally, the increase of R^2 improve the overall fit for all modeled regressions but do not change the overall systematic patterns (Fig. DR6B; Table DR2).

Threshold stochastic stream power incision models (STIMs) and discharge variability

Bedrock channel incision rate, I, is often modeled as a function of the magnitude of the shear stress (or stream power) exerted on a river bed (Howard, 1994). Approximations of this general concept simulate incision as a function of the channel slope, S, raised to an exponent n, upstream drainage area, A, raised to an exponent m, and an erodibility coefficient, K, which captures rock type, climate and downstream changes in the channel hydraulic geometry (Howard, 1994; Whipple and Tucker, 1999):

$$I = KA^m S^n - \psi \quad \text{(DR4)},$$

where ψ is a threshold term for channel incision. Assuming that the incision threshold is negligible and that $I \cong E$ in steady-state basins, equation DR4 is reduced to the constant effective discharge stream power incision model (SPIM) solution (Howard, 1994; Kirby and Whipple, 2012; Lague, 2014):

$$E = KA^m S^n \quad \text{(DR5)}.$$

However, when ψ is significant, the critical discharge needed to overcome the threshold shear stress, Q_c (which is typically defined by the effective bedload grain size), and the distribution of floods are important. Stochastic threshold stream power incision models (or STIMs) account for this via the calculation of E as the integral of the product of I (equation DR4) and the probability of threshold-breaching floods (i.e., floods large enough to generate shear stress capable of exceeding ψ) for specific normalized discharges, $pdf(Q^*)$:

$$Q^* = Q/\overline{Q} \quad \text{(DR6)}$$

$$E = \int_{Q_c}^{Q_{max}} I(Q^*) pdf(Q^*) dQ \quad \text{(DR7)},$$

where Q, $\bar{Q}$, Q^*, and Q_{max} are the actual, mean, normalized, and maximum discharges, respectively (Lague et al., 2005; DiBiase and Whipple, 2011). Lague et al. (2005) present a model where $pdf(Q^*)$ is represented by an inverse gamma distribution:

$$pdf(Q^*) = \frac{k^{k+1}}{\Gamma(k+1)} exp\left(-\frac{k}{Q^*}\right) {Q^*}^{-(2+k)} \quad \text{(DR8)},$$

where Γ is the inverse gamma function, and k is a shape parameter that describes discharge variability. In this model, low to high k reflect heavier-tailed, higher-variability flood distributions to lighter-tailed, lower-variability flood distributions (Lague et al., 2005; Lague, 2014).

This model predicts that in threshold-dominated bedrock river systems, the nonlinearity between E and k_{sn} (equation 1 in main text) systematically increases with decreasing discharge variability (i.e., higher k in equation DR8; Figure 4 in main text). This behavior arises because for steeper channels, smaller magnitude floods are capable of overcoming incision thresholds, while for shallow to moderate channels, small floods are less effective, allowing only larger floods to overcome bedrock incision thresholds (Lague et al., 2005; DiBiase and Whipple, 2011; Deal et al., 2018). The integral of discharge events that breach this incision threshold is related to the erosional efficiency in a STIM framework, where more threshold breaching events increase erosional efficiency. Thus, as channel steepness increases, the flood size needed to breach thresholds declines, and more erosive floods are included in a lighter-tailed, lower discharge flood distribution relative to a heavier-tailed, higher discharge flood distribution system. It is these general concepts that explain why the nonlinearity between E and k_{sn} increases with decreasing discharge variability.

To empirically determine k from discharge records, it is easier to use the complementary cumulative distribution function, $ccdf(Q^*)$, to avoid binning complexities when comparing actual discharge data (DiBiase and Whipple, 2011):

$$ccdf(Q^*) = \Gamma(k/Q^*, k+1) \quad \text{(DR9)}.$$

Empirical studies and theory suggest k to systematically increase with increasing MAP and AI (Lague, 2014; Rossi et al., 2016; Deal et al., 2018). To demonstrate this general pattern at the global scale, we use equation DR9 along with several discharge records near some of our studied basins to empirically determine the shape parameter k for each of these stations and compare it with MAP and AI patterns. We gather mean daily discharge records of ~20-50 years from several gauges near some of our analyzed basins that span a large range of climate conditions (see locations in Figs. 1 in main text, DR1), to calculate their

exceedance probability plots (Fig. DR7A). We calculate similar exceedance probability plots using Lague et al.'s STIM and equation DR9 to verify that STIM predictions generally fit the recorded data (Fig. DR7B). From the STIM exceedance probability plots, we calculate k and compare it with MAP and AI at each gauge station (Fig. 4 in main text; Fig. DR7C; DiBiase and Whipple, 2011; Lague, 2014; Deal et al., 2018).

We find that for the calculated k range using STIMs, p values as a function of the normalized incision threshold, ψ/E, and discharge variability under locally-calibrated parameters (Figure 4 in main text; DiBiase and Whipple, 2011; Lague, 2014) are consistent with empirically derived p from our global analysis (Fig. DR4), where for both cases, p increases from ~1 to 5 with an increase in k from ~0.1 to 3 (GSA DR; Figures 3, 4 in main text, DR7; Molnar et al., 2006; Lague, 2014; Deal et al., 2018). Thus, assuming STIMs are representative for the analyzed basins in this study, our results imply that incision thresholds are important, and that discharge variability decreases with increasing MAP and AI globally.

References

Adams, B.A., Whipple, K.X., Forte, A.M., Heimsath, A.M., and Hodges, K.V., 2020, Climate controls on erosion in tectonically active landscapes: Science Advances, v. 6, p. eaaz3166, doi:10.1126/sciadv.aaz3166.

Amanter, C., and Eakins, B.W., 2009, ETOPO1 arc-minute global relief model: procedures, data sources and analysis.: National Centers for Environmental Information.

Codilean, A.T., Munack, H., Cohen, T.J., Saktura, W.M., Gray, A., and Mudd, S.M., 2018, OCTOPUS: an open cosmogenic isotope and luminescence database: Earth System Science Data, v. 10, p. 2123–2139, doi:10.5194/essd-10-2123-2018.

Deal, E., Braun, J., and Botter, G., 2018, Understanding the Role of Rainfall and Hydrology in Determining Fluvial Erosion Efficiency: Journal of Geophysical Research: Earth Surface, v. 123, p. 744–778, doi:10.1002/2017JF004393.

DiBiase, R.A., and Whipple, K.X., 2011, The influence of erosion thresholds and runoff variability on the relationships among topography, climate, and erosion rate: Journal of Geophysical Research, v. 116, p. F04036, doi:10.1029/2011JF002095.

Fick, S.E., and Hijmans, R.J., 2017, WorldClim 2: new 1-km spatial resolution climate surfaces for global land areas: International Journal of Climatology, v. 37, p. 4302–4315, doi:10.1002/joc.5086.

Flint, J.J., 1974, Stream gradient as a function of order, magnitude, and discharge: Water Resources Research, v. 10, p. 969–973, doi:10.1029/WR010i005p00969.

Gallen, S.F., and Wegmann, K.W., 2017, River profile response to normal fault growth and linkage: an example from the Hellenic forearc of south-central Crete, Greece: Earth Surface Dynamics, v. 5, p. 161–186, doi:10.5194/esurf-5-161-2017.

394 Harel, M.-A., Mudd, S.M., and Attal, M., 2016, Global analysis of the stream power law parameters based
395 on worldwide 10 Be denudation rates: Geomorphology, v. 268, p. 184–196,
396 doi:10.1016/j.geomorph.2016.05.035.

397 Hartmann, J., and Moosdorf, N., 2012, The new global lithological map database GLiM: A representation of
398 rock properties at the Earth surface: Geochemistry, Geophysics, Geosystems, v. 13,
399 doi:10.1029/2012GC004370.

400 Howard, A.D., 1994, A detachment-limited model of drainage basin evolution: Water Resources Research,
401 v. 30, p. 2261–2285, doi:10.1029/94WR00757.

402 Kirby, E., and Whipple, K.X., 2012, Expression of active tectonics in erosional landscapes: Journal of
403 Structural Geology, v. 44, p. 54–75, doi:10.1016/j.jsg.2012.07.009.

404 Lague, D., 2014, The stream power river incision model: evidence, theory and beyond: Earth Surface
405 Processes and Landforms, v. 39, p. 38–61, doi:10.1002/esp.3462.

406 Lague, D., Hovius, N., and Davy, P., 2005, Discharge, discharge variability, and the bedrock channel profile:
407 Journal of Geophysical Research: Earth Surface, v. 110, p. n/a-n/a, doi:10.1029/2004JF000259.

408 Perron, J.T., Royden, L., Niemi, N.A., Schildgen, T.F., Van Der Beek, P.A., Sinclair, H.D., and Thiede, R.C., 2013,
409 An integral approach to bedrock river profile analysis: Earth Surface Processes and Landforms, v.
410 38, p. 570–576, doi:10.1002/esp.3302.

411 Rossi, M.W., Whipple, K.X., and Vivoni, E.R., 2016, Precipitation and evapotranspiration controls on daily
412 runoff variability in the contiguous United States and Puerto Rico: Journal of Geophysical Research:
413 Earth Surface, v. 121, p. 128–145, doi:10.1002/2015JF003446.

414 Royden, L., and Taylor Perron, J., 2013, Solutions of the stream power equation and application to the
415 evolution of river longitudinal profiles: Journal of Geophysical Research: Earth Surface, v. 118, p.
416 497–518, doi:10.1002/jgrf.20031.

417 Schwanghart, W., and Scherler, D., 2014, Short Communication: TopoToolbox 2 – MATLAB-based software
418 for topographic analysis and modeling in Earth surface sciences: Earth Surface Dynamics, v. 2, p. 1–
419 7, doi:10.5194/esurf-2-1-2014.

420 Snyder, N.P., Whipple, K.X., Tucker, G.E., and Merritts, D.J., 2000, Landscape response to tectonic forcing:
421 Digital elevation model analysis of stream profiles in the Mendocino triple junction region, northern
422 California: Geological Society of America Bulletin, v. 112, p. 1250–1263.

423 Trabucco, A., and Zomer, R.J., 2009, Global aridity index (global-aridity) and global potential evapo-
424 transpiration (global-PET) geospatial database.: CGIAR Consortium for Spatial Information, v. 89, p.
425 1–2.

426 Whipple, K.X., Forte, A.M., DiBiase, R.A., Gasparini, N.M., and Ouimet, W.B., 2017, Timescales of landscape
427 response to divide migration and drainage capture: Implications for the role of divide mobility in
428 landscape evolution: Landscape Response to Divide Mobility: Journal of Geophysical Research:
429 Earth Surface, v. 122, p. 248–273, doi:10.1002/2016JF003973.

Whipple, K.X., and Tucker, G.E., 1999, Dynamics of the stream-power river incision model: Implications for height limits of mountain ranges, landscape response timescales, and research needs: Journal of Geophysical Research: Solid Earth, v. 104, p. 17661–17674, doi:10.1029/1999JB900120.

Willett, S.D., McCoy, S.W., Perron, J.T., Goren, L., and Chen, C.-Y., 2014, Dynamic Reorganization of River Basins: Science, v. 343, p. 1248765–1248765, doi:10.1126/science.1248765.

Wobus, C., Whipple, K.X., Kirby, E., Snyder, N., Johnson, J., Spyropolou, K., Crosby, B., and Sheehan, D., 2006, Tectonics from topography: Procedures, promise, and pitfalls, *in* Tectonics, Climate, and Landscape Evolution, Geological Society of America, doi:10.1130/2006.2398(04).

Figure and table captions

Figure DR1: Global climate rasters used for our analysis. **(A)** Mean annual precipitation (MAP; 'WorldClim 2'; Fick and Hijmans, 2017) **(B)** Mean annual temperature (MAT; 'WorldClim 2'; Fick and Hijmans, 2017); **(C)** Aridity index (AI; 'CGIAR-CSI'; Trabucco and Zomer, 2009); **(D)** Elevation (ME; 'ETOPO1'; Amanter and Eakins, 2009). Marked are the locations of the analyzed basin regions (red stars) and stream gauge stations in Figure DR7 (cyan marks).

Figure DR2: **(A)** Global rock type data (after 'GLiM'; Hartmann and Moosdorf, 2012) classified by crystalline, volcanic, and sedimentary rocks, where crystalline rocks consist of plutonic and metamorphic units. All analyzed basins in this study consist of at least 90% crystalline units. **(B)** Binned data of the percentages of plutonic and metamorphic units for 265 basins under a steady state threshold of $R^2 > 0.9$, versus MAP, MAT, AI, and ME (Table DR1). At the global scale, no relationship is observed between changes in the percentage of plutonic or metamorphic units and climate variability.

Figure DR3: **(A)** Modeled regressions for k_{sn} versus E (equation 1 in main text) for 265 basins under a steady state threshold of $R^2 > 0.9$, where each data point represents one basin. Data is classified and binned by (from top left clockwise) MAP, MAT, AI, and ME (see Table DR1). Legend shows statistical goodness-of-fit parameters (R^2, χ^2,KS test p-value) for each climate bin modeled regression (see Table DR2). **(B)** Same as (A) but for $k_{sn}Q$, where MAP across the basin is weighted in drainage area prior to calculation of χ (see text). The regressions and associated data points with low or negative R^2 or KS test p-value < 0.1 are colored in transparent grey (see also Table DR2).

Figure DR4: **(A)** Values of p in equation 1 for each modeled regression for k_{sn} and $k_{sn}Q$ under changes in MAP, MAT, AI, and ME. Note a systematic increase in p with increasing MAP (i.e., wetter) and AI (i.e., higher humidity). **(B)** Same as (A) but for C in equation 1. Note a systematic decrease in C with

increasing MAP and AI. For all regressions, $k_{sn}Q$ does not significantly change systematic patterns. For both (A) and (B), associated p and C with low or negative R^2 or p-value < 0.1 are transparent (see also Table DR2).

Figure DR5: (A) Modeled normalized regressions for k_{sn} versus E (equation 1 in main text) under a fixed p = 2.2, which is the global value from best fit regression through the entire E - k_{sn} dataset. Regressions and associated data points with low or negative R^2 or p-value < 0.1 are colored in transparent grey (see also Table DR2). **(B)** Changes in C_{ne} under a fixed p = 2.2. Note that C_{ne} generally decreases from ~$10^{-8}$$m^{-7}$$yr^{-1}$ to $10^{-9}$$m^{-8}$$yr^{-1}$ with all climate proxies. $k_{sn}Q$ does not significantly change systematic patterns. Associated C_{ne} with low or negative R^2 or p-value < 0.1 are transparent (see Table DR2).

<u>Figure DR6:</u> Sensitivity analyses for modeled regressions under **(A)** changes of the number of bins and **(B)** changes of the R^2 threshold used to define morphological steady state (e.g., Figure 1, inset in main text). p (and hence C that covary with it; Figure DR4) is statistically robust to changes in MAP and AI under different number of bins and R^2 threshold values and to changes in ME and MAT under different R^2 threshold values. For both (A) and (B), associated p with low or negative R^2 or p-value < 0.1 are transparent (see also Table DR2).

Figure DR7: (A) Exceedance probability plots of normalized recorded mean daily discharge (m^3/s), Q^* (equation DR6), from seven stream gauge stations with records spanning ~20-50 yrs near some of our analyzed basins (for locations, see Figs. 1 in main text, DR1). **(B)** Exceedance probability plots based on modeled cumulative distribution function of the normalized discharge, $ccdf(Q^*)$ (equation DR9), where low to high k represents high to low discharge variability (Lague et al., 2005; DiBiase and Whipple, 2011; Deal et al., 2018). Note a general systematic decrease in discharge variability (higher k) with increasing MAP and AI. **(C)** MAP and AI as a function of k based on (A) and (B).

Table DR1: Locations, climate proxy values, erosion rates, k_{sn}, $k_{sn}Q$, and percentage of crystalline units for 265 analyzed basins under a morphological steady-state threshold of R^2 > 0.9.

Table DR2: p, C, C_{ne} and statistical goodness-of-fit metrics of R^2, χ^2, and Kolmogorov-Smirnov two-sided p-value at the 90% significance level for six climate bins of MAP, MAT, AI, and ME under different R^2 morphological steady-state thresholds from 0.75 to 0.95. Bolded values are low or negative R^2 or Kolmogorov-Smirnov p-value < 0.1 of poorly fit regressions.

Figure DR1

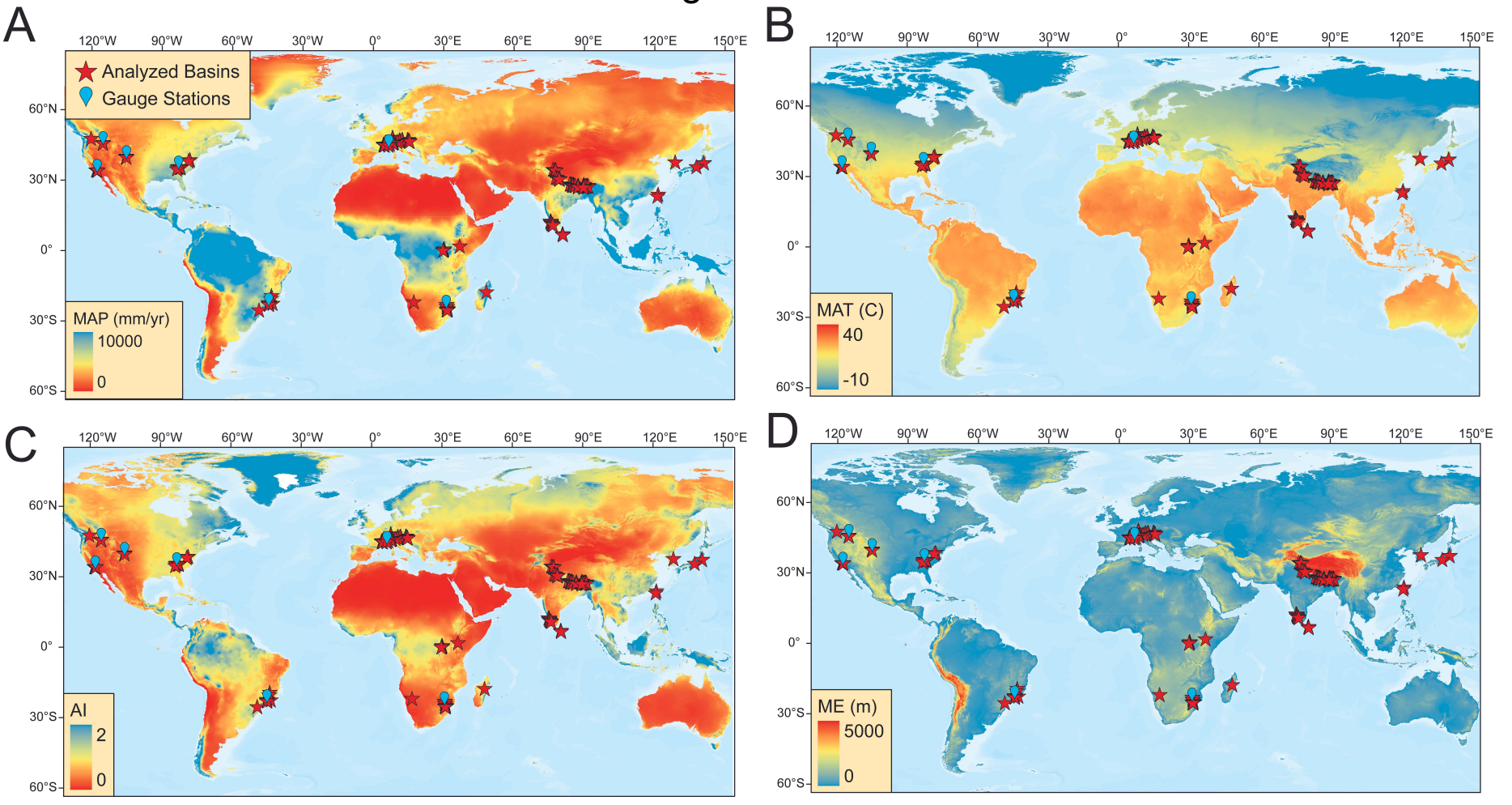
A
Analyzed Basins
Gauge Stations
MAP (mm/yr)
10000
0
B
MAT (C)
40
-10
C
AI
2
0
D
ME (m)
5000
0
120°W
90°W
60°W
30°W
0°
30°E
60°E
90°E
120°E
150°E
60°N
30°N
0°
30°S
60°S

Figure DR2

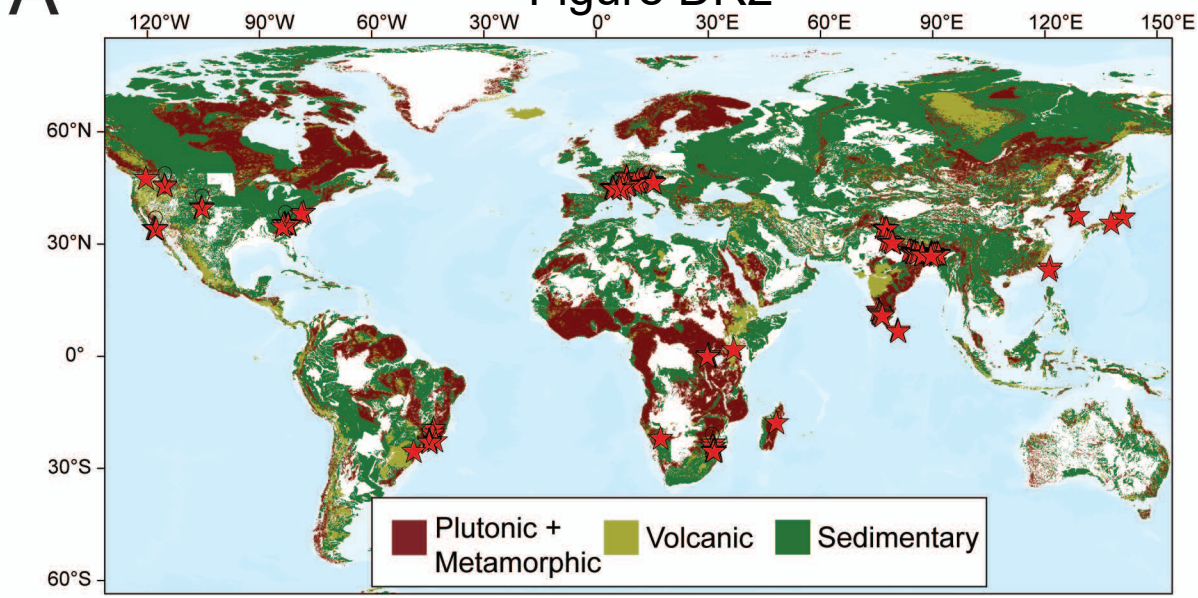
A
120°W
90°W
60°W
30°W
0°
30°E
60°E
90°E
120°E
150°E
60°N
30°N
0°
30°S
60°S
Plutonic + Metamorphic
Volcanic
Sedimentary

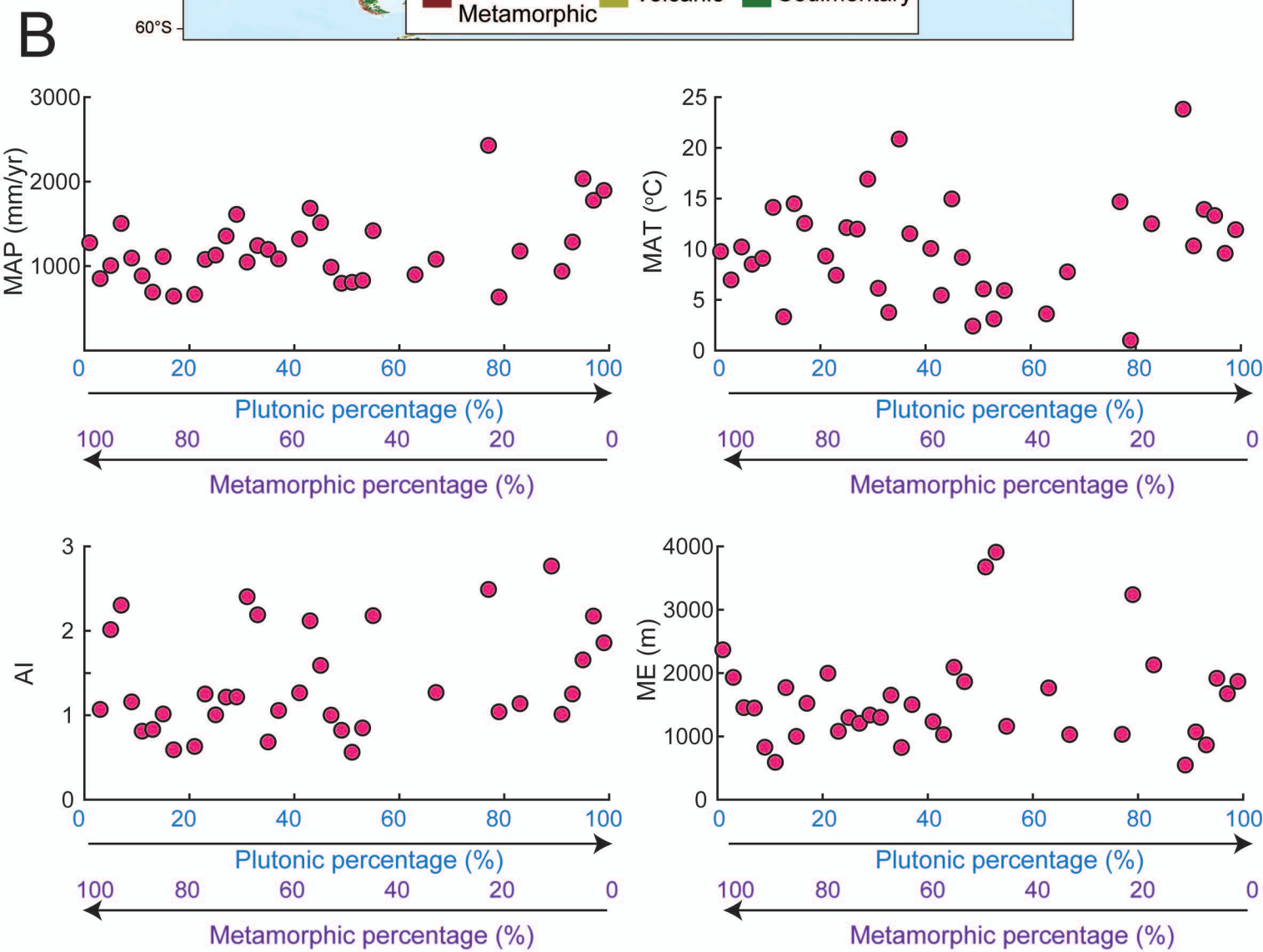
B
MAP (mm/yr)
3000
2000
1000
MAT (°C)
25
20
15
10
5
0
AI
3
2
1
0
ME (m)
4000
3000
2000
1000
0
20
40
60
80
100
Plutonic percentage (%)
Metamorphic percentage (%)

Figure DR3

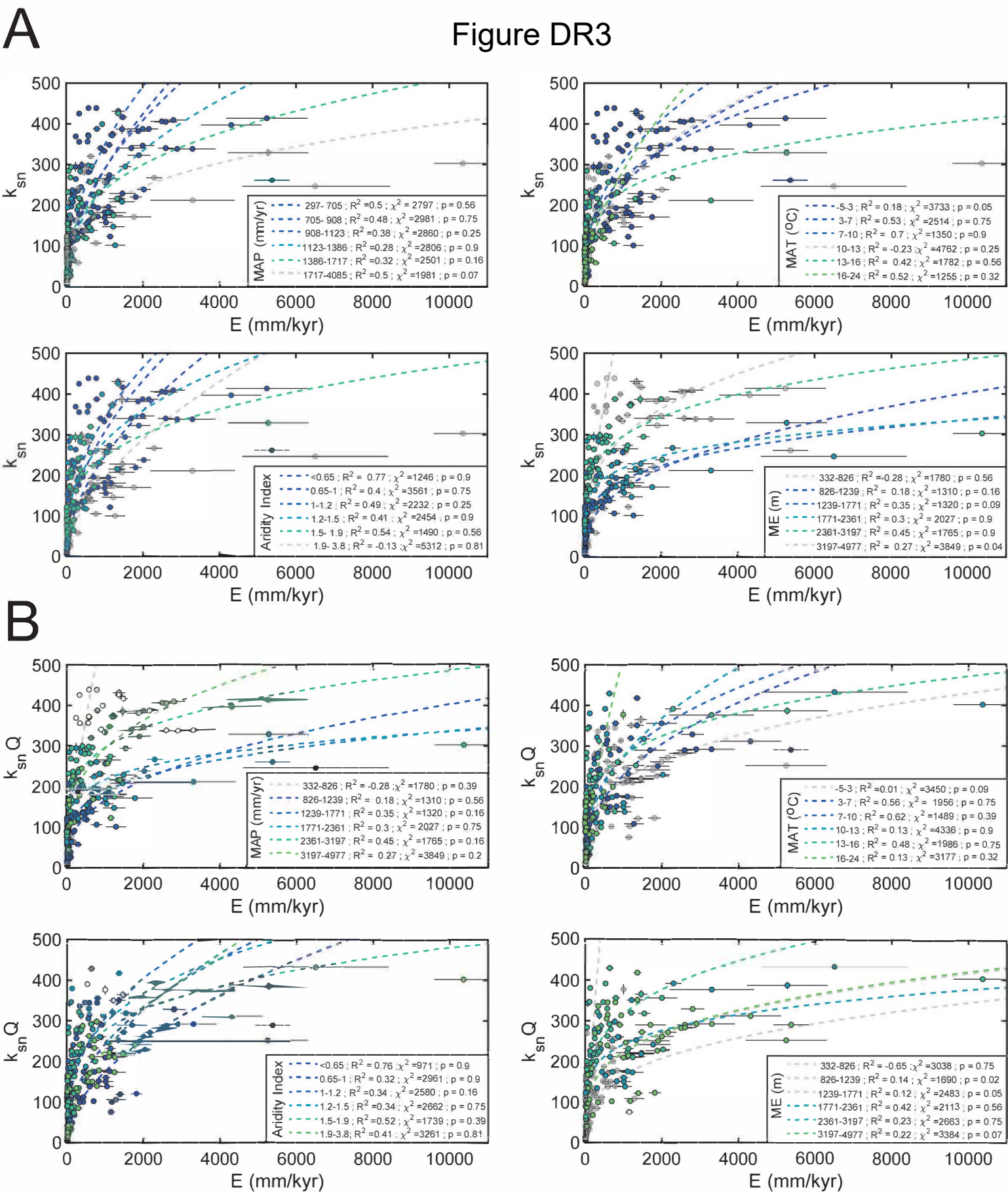
A
B
k_{sn}
$k_{sn}Q$
E (mm/kyr)
MAP (mm/yr)
297- 705 ; R^2 =0.5 ; χ^2 = 2797 ; p = 0.56
705- 908 ; R^2 =0.48 ; χ^2 =2981 ; p = 0.75
908-1123 ; R^2 =0.38 ; χ^2 =2860 ; p = 0.25
1123-1386 ; R^2 =0.28 ; χ^2 =2806 ; p = 0.9
1386-1717 ; R^2 =0.32 ; χ^2 =2501 ; p = 0.16
1717-4085 ; R^2 =0.5 ; χ^2 =1981 ; p = 0.07
MAT (°C)
-5-3 ; R^2 = 0.18 ; χ^2 =3733 ; p = 0.05
3-7 ; R^2 = 0.53 ; χ^2 =2514 ; p = 0.75
7-10 ; R^2 = 0.7 ; χ^2 =1350 ; p =0.9
10-13 ; R^2 = -0.23 ; χ^2 =4762 ; p = 0.25
13-16 ; R^2 = 0.42 ; χ^2 =1782 ; p = 0.56
16-24 ; R^2 = 0.52 ; χ^2 =1255 ; p = 0.32
Aridity Index
<0.65 ; R^2 = 0.77 ; χ^2 =1246 ; p = 0.9
0.65-1 ; R^2 = 0.4 ; χ^2 =3561 ; p = 0.75
1-1.2 ; R^2 = 0.49 ; χ^2 =2232 ; p = 0.25
1.2-1.5 ; R^2 = 0.41 ; χ^2 =2454 ; p = 0.9
1.5- 1.9 ; R^2 = 0.54 ; χ^2 =1490 ; p = 0.56
1.9- 3.8 ; R^2 = -0.13 ; χ^2 =5312 ; p = 0.81
ME (m)
332-826 ; R^2 =-0.28 ; χ^2 =1780 ; p = 0.56
826-1239 ; R^2 = 0.18 ; χ^2 =1310 ; p = 0.16
1239-1771 ; R^2 = 0.35 ; χ^2 =1320 ; p = 0.09
1771-2361 ; R^2 = 0.3 ; χ^2 = 2027 ; p = 0.9
2361-3197 ; R^2 = 0.45 ; χ^2 =1765 ; p = 0.9
3197-4977 ; R^2 = 0.27 ; χ^2 =3849 ; p = 0.04
MAP (mm/yr)
332-826 ; R^2 = -0.28 ; χ^2 =1780 ; p = 0.39
826-1239 ; R^2 = 0.18 ; χ^2 =1310 ; p = 0.56
1239-1771 ; R^2 = 0.35 ; χ^2 =1320 ; p = 0.16
1771-2361 ; R^2 = 0.3 ; χ^2 = 2027 ; p = 0.75
2361-3197 ; R^2 = 0.45 ; χ^2 =1765 ; p = 0.16
3197-4977 ; R^2 = 0.27 ; χ^2 =3849 ; p = 0.2
MAT (°C)
-5-3 ; R^2 =0.01 ; χ^2 =3450 ; p = 0.09
3-7 ; R^2 = 0.56 ; χ^2 = 1956 ; p = 0.75
7-10 ; R^2 = 0.62 ; χ^2 =1489 ; p = 0.39
10-13 ; R^2 = 0.13 ; χ^2 =4336 ; p = 0.9
13-16 ; R^2 = 0.48 ; χ^2 =1986 ; p = 0.75
16-24 ; R^2 = 0.13 ; χ^2 =3177 ; p = 0.32
Aridity Index
<0.65 ; R^2 = 0.76 ; χ^2 =971 ; p = 0.9
0.65-1 ; R^2 = 0.32 ; χ^2 =2961 ; p = 0.9
1-1.2 ; R^2 =0.34 ; χ^2 =2580 ; p = 0.16
1.2-1.5 ; R^2 =0.34 ; χ^2 =2662 ; p = 0.75
1.5-1.9 ; R^2 =0.52 ; χ^2 =1739 ; p = 0.39
1.9-3.8; R^2 =0.41 ; χ^2 =3261 ; p = 0.81
ME (m)
332-826 ; R^2 = -0.65 ; χ^2 =3038 ; p = 0.75
826-1239 ; R^2 = 0.14 ; χ^2 =1690 ; p = 0.02
1239-1771 ; R^2 = 0.12 ; χ^2 =2483 ; p = 0.05
1771-2361 ; R^2 = 0.42 ; χ^2 =2113 ; p = 0.56
2361-3197 ; R^2 = 0.23 ; χ^2 =2663 ; p = 0.75
3197-4977 ; R^2 = 0.22 ; χ^2 =3384 ; p = 0.07

Figure DR4

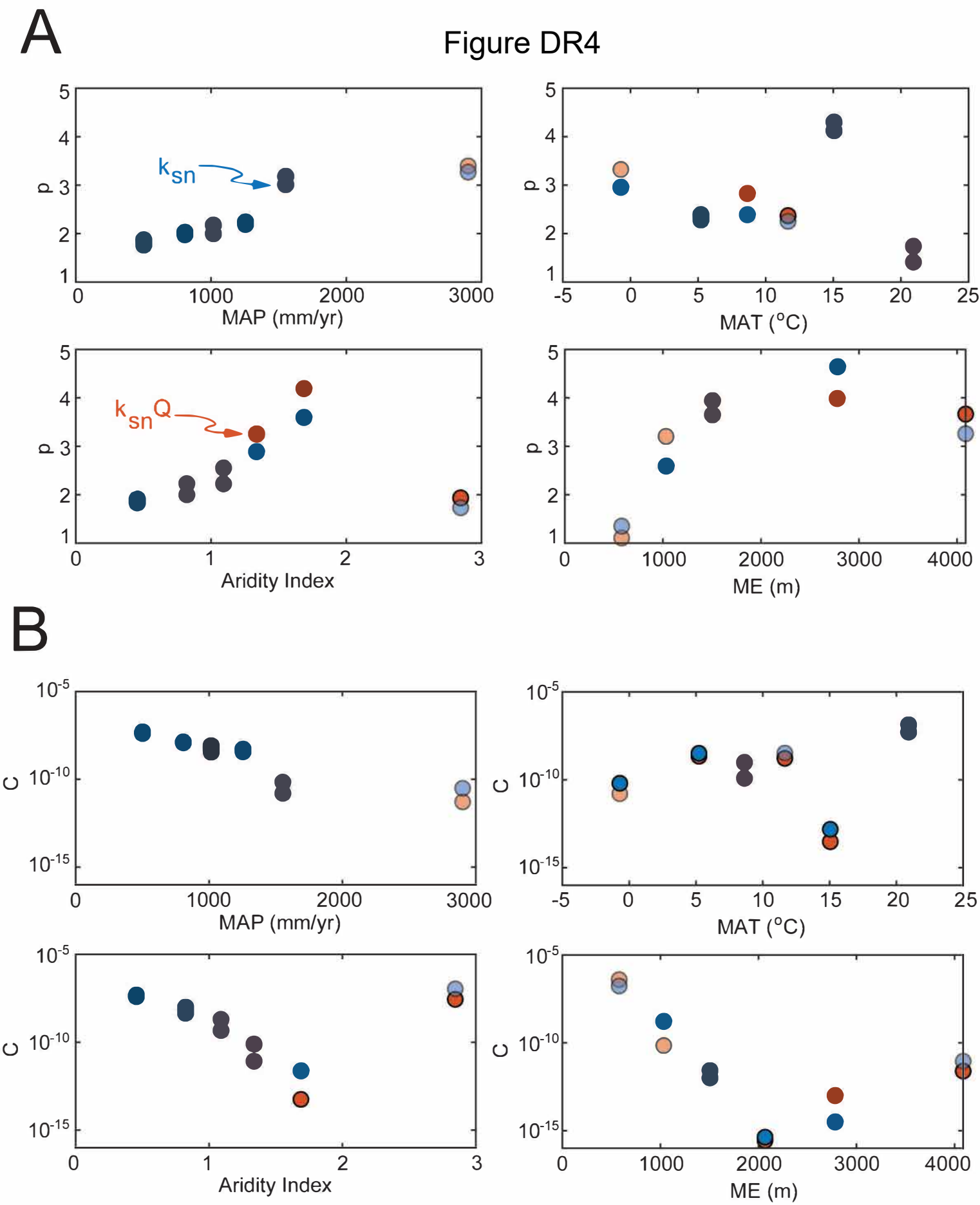
A
p
MAP (mm/yr)
MAT (°C)
Aridity Index
ME (m)
k_{sn}
$k_{sn}Q$
B
C
MAP (mm/yr)
MAT (°C)
Aridity Index
ME (m)

Figure DR5

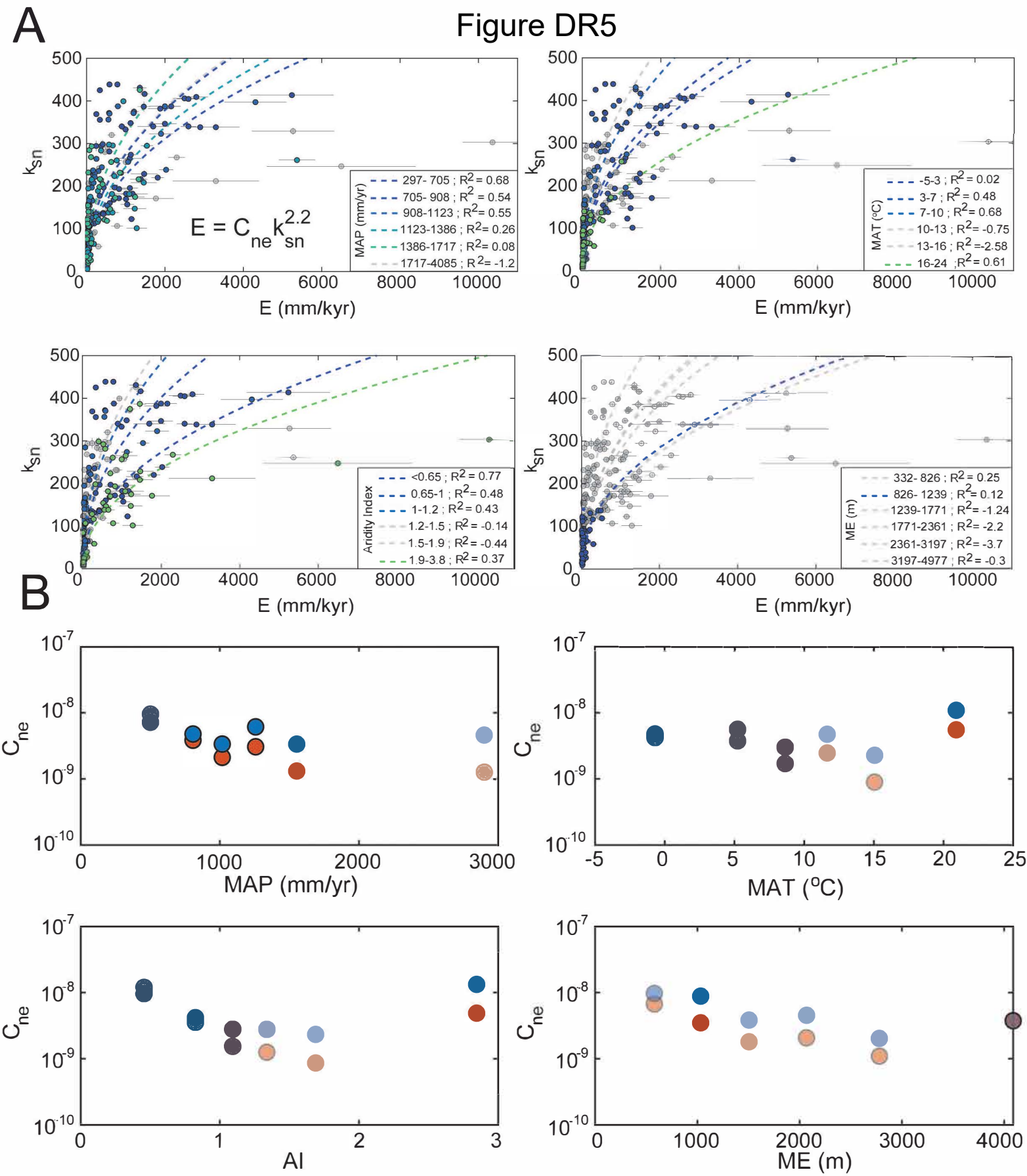
A
B
E = C_ne k_sn^2.2
k_sn
E (mm/kyr)
MAP (mm/yr)
297- 705 ; R2 = 0.68
705- 908 ; R2 = 0.54
908-1123 ; R2= 0.55
1123-1386 ; R2= 0.26
1386-1717 ; R2= 0.08
1717-4085 ; R2= -1.2
MAT (°C)
-5-3 ; R2 = 0.02
3-7 ; R2 = 0.48
7-10 ; R2= 0.68
10-13 ; R2= -0.75
13-16 ; R2 =-2.58
16-24 ; R2= 0.61
Aridity Index
<0.65 ; R2 = 0.77
0.65-1 ; R2= 0.48
1-1.2 ; R2= 0.43
1.2-1.5 ; R2 = -0.14
1.5-1.9 ; R2 = -0.44
1.9-3.8 ; R2 = 0.37
ME (m)
332- 826 ; R2 = 0.25
826- 1239 ; R2= 0.12
1239-1771 ; R2= -1.24
1771-2361 ; R2= -2.2
2361-3197 ; R2= -3.7
3197-4977 ; R2= -0.3
C_ne
MAP (mm/yr)
MAT (°C)
AI
ME (m)

Figure DR6

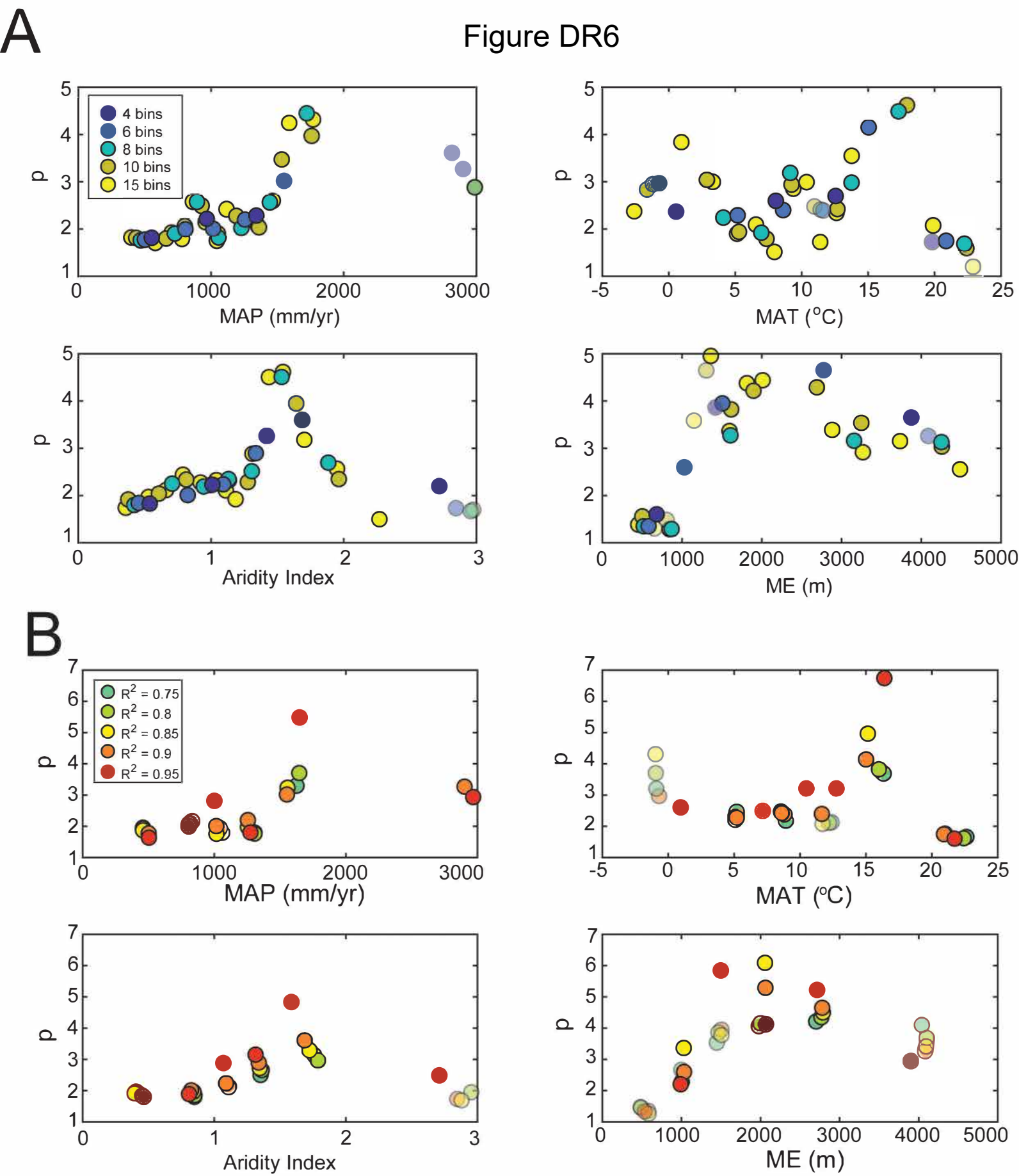
A
4 bins
6 bins
8 bins
10 bins
15 bins
p
MAP (mm/yr)
MAT (°C)
Aridity Index
ME (m)
B
R2 = 0.75
R2 = 0.8
R2 = 0.85
R2 = 0.9
R2 = 0.95
p
MAP (mm/yr)
MAT (ºC)
Aridity Index
ME (m)

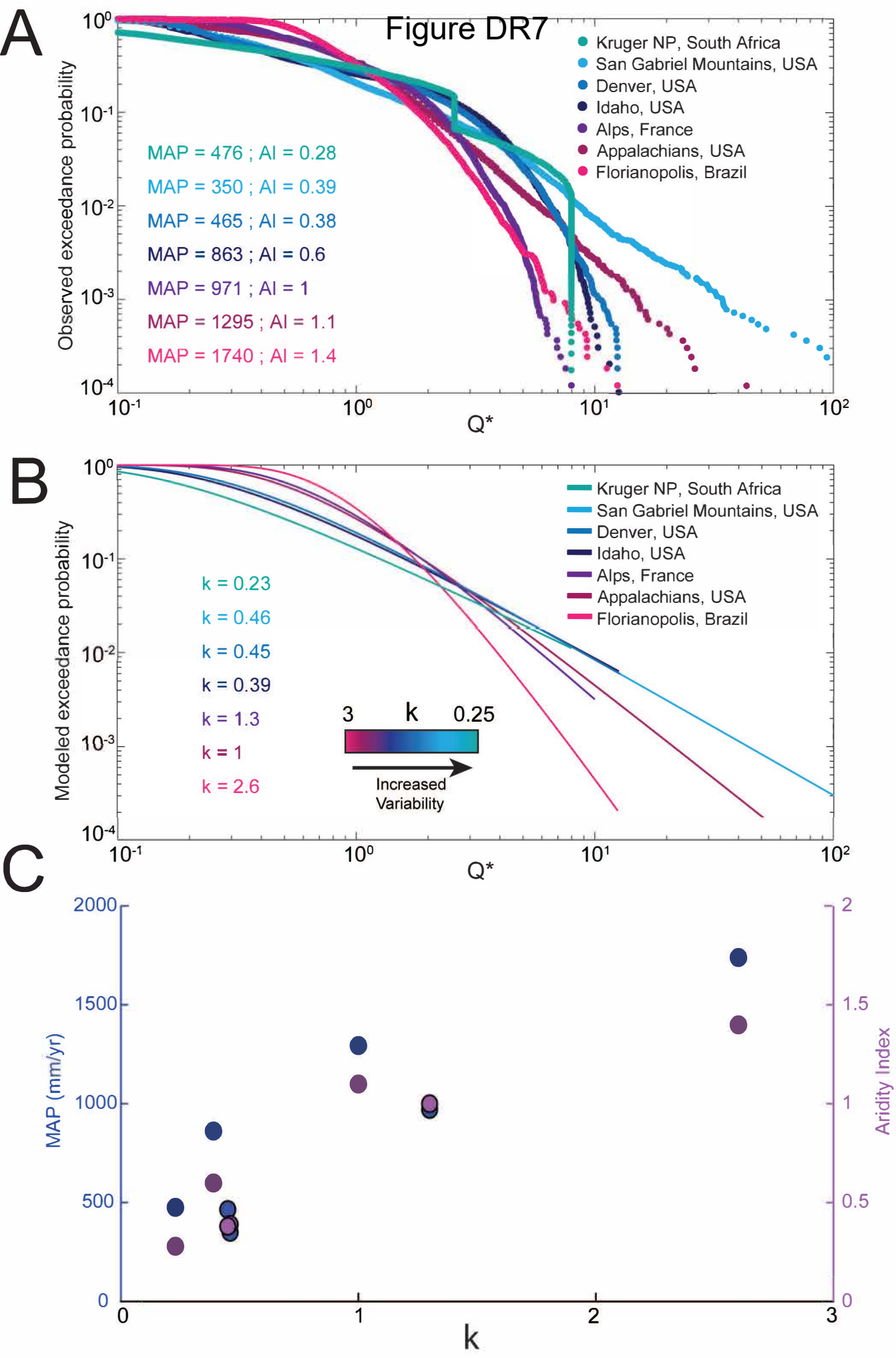
Figure DR7
A
Observed exceedance probability
Q*
Kruger NP, South Africa
San Gabriel Mountains, USA
Denver, USA
Idaho, USA
Alps, France
Appalachians, USA
Florianopolis, Brazil
MAP = 476 ; AI = 0.28
MAP = 350 ; AI = 0.39
MAP = 465 ; AI = 0.38
MAP = 863 ; AI = 0.6
MAP = 971 ; AI = 1
MAP = 1295 ; AI = 1.1
MAP = 1740 ; AI = 1.4
B
Modeled exceedance probability
Q*
k = 0.23
k = 0.46
k = 0.45
k = 0.39
k = 1.3
k = 1
k = 2.6
3 k 0.25
Increased Variability
C
MAP (mm/yr)
Aridity Index
k

Table DR1

TABLE DR1. ANALYZED BASIN LOCATIONS, CLIMATE PROXIES, TOPOGRAPHIC METRICS, AND ROCK TYPE

Global Zone	Basin ID	Publication	Latitude (WGS84)	Longtitude (WGS84)	MAP (mm/yr)		MAT (°C)		AI		ME (m)		E (m/My)		Ksn ($m^{0.9}$)		KsnQ ($m^{0.9}$)		Crystalline Area (%)	
					Mean	STD	Mean	STD	Mean	STD	Mean	STD	Mean	STD	Mean	STD	Mean	STD	Plut.	Meta.
App	2	Duxburry, 2008	-78.24	38.65	1102	43	11	1	1.04	0.1	551	175	17	2	58.37	1.03	61.49	1.13	10	83
App	4	Duxburry, 2008	-78.26	38.61	1147	39	10	1	1.12	0.09	688	147	16	2	82.79	2.02	88.69	2.14	10	90
App	5	Duxburry, 2008	-78.29	38.57	1152	54	10	1	1.13	0.12	697	200	17	2	94.56	1.42	101.9	1.56	21	75
App	7	Duxburry, 2008	-78.79	38.2	1152	54	10	1	1.13	0.12	697	200	15	2	94.56	1.42	101.9	1.56	0	100
App	13	Matmon, 2003	-83.13	35.74	1127	26	11	0	1.04	0.05	639	108	14	2	25.45	0.66	27.01	0.72	0	97
App	16	Matmon, 2003	-83.25	35.61	1163	16	12	1	0.97	0.05	543	150	11	1	27.59	1.07	29.54	1.16	0	90
App	20	Sullivan, 2007	-82.22	35.57	1275	35	13	1	1.13	0.15	633	240	25	2	34.07	0.5	38.1	0.57	0	100
App	21	Linari, 2016	-82.22	35.57	1625	150	9	1	1.6	0.26	1306	258	34	4	125.69	1.8	160.1	2.17	0	100
App	22	Matmon, 2003	-83.25	35.56	1654	130	9	1	1.65	0.24	1349	232	33	4	108.39	1.39	138.7	1.68	0	100
App	23	Linari, 2016	-82.38	35.54	1319	40	13	1	1.1	0.08	673	160	29	2	48.44	1.9	55.29	2.2	0	100
App	24	Sullivan, 2007	-82.38	35.54	1319	39	13	1	1.1	0.08	674	155	23	3	51.38	1.98	58.69	2.29	0	100
App	25	Matmon, 2003	-83.31	35.52	1791	49	9	1	1.86	0.13	1517	139	19	3	53.72	0.82	70.25	1.06	0	100
App	26	Matmon, 2003	-83.29	35.52	1314	28	13	0	1.07	0.05	587	118	18	2	22.84	1.3	25.88	1.49	0	93
App	27	Matmon, 2003	-83.3	35.51	1314	28	13	0	1.07	0.05	588	120	23	2	21.11	1.35	23.91	1.54	0	90
App	28	Matmon, 2003	-83.57	35.47	1770	71	9	1	1.81	0.16	1464	175	19	2	103.24	2.97	134.8	3.84	0	97
App	30	Matmon, 2003	-83.43	35.46	1340	29	13	0	1.12	0.05	706	114	32	2	44.74	1.41	51.15	1.64	0	94
App	31	Matmon, 2003	-83.53	35.46	1687	120	10	1	1.61	0.22	1249	225	23	3	93.55	1.29	120.5	1.74	0	100
App	32	Linari, 2016	-82.18	35.34	1412	58	12	1	1.24	0.11	915	136	16	1	30.79	1.29	36.34	1.56	0	100
App	33	Sullivan, 2007	-82.18	35.34	1395	43	12	0	1.2	0.08	874	98	13	2	21.12	0.55	24.62	0.65	0	100
App	34	Linari, 2016	-82.32	35.32	1595	92	11	1	1.42	0.15	1021	181	23	3	78.22	0.78	98.01	0.97	7	93
App	37	Reusser, 2015	-83.77	34.74	1661	129	10	1	1.58	0.25	1226	270	28	4	81.29	0.52	103.9	0.69	0	100
CUS	3	Kirchner, 2001	-115.34	45.99	684	7	5	0	0.81	0.03	1566	105	32	4	51.86	0.9	43.77	0.76	0	100
CUS	4	Kirchner, 2001	-115.33	45.99	684	5	4	0	0.82	0.04	1594	118	28	4	60.4	2.04	50.92	1.72	0	100
CUS	8	Kirchner, 2001	-115.34	45.71	692	19	3	1	0.83	0.06	1771	170	21	3	69.4	0.53	58.68	0.47	12	88
CUS	9	Kirchner, 2001	-115.33	45.67	666	13	3	0	0.81	0.02	1769	104	21	3	44.27	0.74	36.67	0.61	3	97
CUS	12	Foster, 2016	-105.47	40.16	502	31	3	1	0.65	0.1	2787	169	16	1	80.65	3.74	59.5	2.91	99	0
CUS	13	Dethier, 2014	-105.53	39.96	502	31	3	1	0.65	0.1	2787	169	19	2	80.65	3.74	59.5	2.91	46	51
CUS	14	Dethier, 2014	-105.35	39.86	633	88	1	1	1.04	0.26	3239	300	38	3	104.71	0.94	87.89	0.8	79	21
CUS	15	Dethier, 2014	-105.33	39.74	486	23	4	1	0.62	0.09	2718	179	18	2	89.3	3.13	65.37	2.24	0	100
Pac	4	Moon, 2011	-120.37	47.74	937	235	4	2	1.23	0.43	1332	350	127	9	125.95	0.87	130.3	0.78	47	53
Pac	10	DiBiase, 2010	-118.12	34.33	532	65	14	1	0.47	0.08	1355	180	135	33	64.59	0.44	49.92	0.44	90	10
Pac	13	DiBiase, 2010	-117.73	34.31	766	58	10	2	0.73	0.11	2022	420	1106	204	195.82	2.06	175.9	1.88	2	98
Pac	14	DiBiase, 2010	-117.73	34.31	744	47	10	1	0.69	0.08	1950	345	1039	175	157.41	1.42	138.6	1.24	4	96
Pac	16	DiBiase, 2010	-117.98	34.31	705	59	12	1	0.67	0.1	1728	297	239	28	135.26	3.77	117.4	3.39	100	0
Pac	17	DiBiase, 2010	-117.76	34.3	768	31	10	1	0.73	0.07	1951	317	1006	191	170.07	2.29	150.9	2.01	24	76
Pac	18	DiBiase, 2010	-118.26	34.3	474	55	14	1	0.41	0.06	1149	242	424	37	137.44	1.63	100.8	1.11	83	17
Pac	19	DiBiase, 2010	-117.74	34.3	750	60	10	2	0.71	0.1	1964	389	436	50	197.1	2.3	174.6	2.02	14	86

Pac	20	DiBiase, 2010	-117.74	34.3	750	60	10	2	0.71	0.1	1964	389	717	106	197.1	2.3	174.6	2.02	3	97
Pac	21	DiBiase, 2010	-117.89	34.27	746	61	10	1	0.69	0.1	1954	382	826	79	172.13	1.85	152.2	1.73	100	0
Pac	22	DiBiase, 2010	-117.89	34.27	656	134	12	1	0.59	0.13	1532	364	591	84	160.57	1.23	138.3	1.09	100	0
Pac	23	DiBiase, 2010	-117.97	34.25	613	143	13	1	0.55	0.14	1404	361	428	85	134.9	2.01	112.4	2.05	93	7
Pac	24	DiBiase, 2010	-117.76	34.24	644	110	13	1	0.59	0.13	1523	339	292	37	131.66	1.44	111.9	1.28	16	84
Pac	25	DiBiase, 2010	-117.64	34.16	706	121	11	2	0.66	0.13	1809	477	1010	108	182.72	1.22	160.4	1.11	47	52
Alps	1	Meyer, 2010	8.21	48.24	1347	116	7	1	1.56	0.23	788	169	91	7	85.97	0.84	100.1	1.02	87	8
Alps	6	Morel, 2003	8.2	47.94	1487	81	6	0	1.96	0.1	989	69	43	5	19.95	0.68	24.16	0.82	0	100
Alps	8	Morel, 2003	8.16	47.88	1685	73	5	0	2.12	0.17	1028	78	73	10	28.87	0.82	36.85	1.05	43	57
Alps	9	Morel, 2003	8.26	47.87	1524	158	6	0	2	0.24	983	105	47	6	24.65	0.29	30.6	0.38	14	82
Alps	10	Morel, 2003	8.22	47.86	1587	119	6	0	2.02	0.17	987	87	110	15	26.52	0.59	33.38	0.75	52	43
Alps	17	Dixon, 2016	14.66	47.27	1494	186	3	1	2.37	0.39	1588	299	77	5	107.04	1.68	131.9	2.08	0	99
Alps	18	Norton, 2011	12.42	47.27	1333	150	2	2	2.41	0.75	1956	467	1090	470	181.96	3.32	211.7	3.86	3	97
Alps	19	Norton, 2011	11.26	47.25	1333	150	2	2	2.41	0.75	1956	467	650	110	181.96	3.32	211.7	3.86	0	99
Alps	22	Dixon, 2016	14.78	47.15	1246	141	0	3	2.95	1.17	2238	513	710	130	224.01	2.32	251.3	2.6	0	98
Alps	25	Norton, 2011	12.13	47.05	1458	113	-1	2	3.25	1.1	2363	414	1240	240	174.93	3.18	210.5	3.82	32	68
Alps	26	Dixon, 2016	14.82	46.94	1384	100	-1	2	3.04	0.78	2351	335	1230	290	147.51	2.86	173.4	3.4	0	94
Alps	28	Dixon, 2016	15.17	46.84	1080	154	1	3	2.45	1.07	2085	469	530	100	154.41	2.02	165.5	2.17	0	100
Alps	29	Dixon, 2016	15.18	46.82	1229	123	5	1	1.73	0.26	1144	271	57	3	93.69	1.05	104.7	1.25	0	100
Alps	32	Savi, 2014	11.02	46.72	861	44	2	2	1.84	0.43	1907	321	376	70	294.49	12.22	277.6	11.23	0	100
Alps	33	Savi, 2014	11.02	46.72	861	44	2	2	1.84	0.43	1907	321	246	42	294.49	12.22	277.6	11.23	0	100
Alps	34	Savi, 2014	11.03	46.71	895	54	2	2	2.07	0.56	2012	387	1470	340	228.82	8.08	220.8	7.63	0	100
Alps	42	Savi, 2014	11.07	46.67	832	156	-2	2	3.56	1.19	2559	366	412	26	298.59	9.93	287.1	8.87	0	99
Alps	44	Dixon, 2016	15.14	46.61	790	161	0	3	3.11	1.39	2368	537	1460	160	386.75	11.3	365.3	10.02	0	100
Alps	46	Dixon, 2016	15.43	46.53	790	160	0	3	3.09	1.4	2353	559	1210	120	374.92	8.07	350.8	7.07	5	95
Alps	47	Wittmann, 2007	8.64	46.41	770	213	0	3	3.21	1.6	2362	534	580	110	281.45	3.05	262.4	2.67	0	92
Alps	49	Norton, 2011	10.25	46.33	1284	126	5	2	1.79	0.29	1184	307	69	6	118.47	0.95	136	1.05	0	91
Alps	50	Wittmann, 2007	8.71	46.25	593	176	-1	3	3.22	1.57	2424	535	1100	300	265.4	2.77	221.8	2	0	100
Alps	54	Wittmann, 2007	8.7	46.17	1369	90	2	2	3.71	1.01	1964	441	770	130	260.66	7.39	297.9	8.29	7	92
Alps	57	Wittmann, 2007	8.26	46.02	1431	63	4	2	2.89	0.74	1646	454	590	120	146.64	3.09	171.8	3.61	7	93
Alps	58	Wittmann, 2016	8.53	45.96	1431	63	4	2	2.89	0.74	1646	454	600	110	146.64	3.09	171.8	3.61	0	100
Alps	59	Wittmann, 2007	8.26	45.81	1251	70	6	2	2.35	0.58	1333	441	560	100	138.39	1.53	150.5	1.74	5	92
Alps	60	Glotzbach, 2013	6.14	45.41	1251	70	6	2	2.35	0.58	1333	441	660	160	138.39	1.53	150.5	1.74	54	43
Alps	62	Glotzbach, 2013	6.26	45.39	1131	83	2	3	3.8	1.44	1930	605	1460	330	208.61	1.38	218.6	1.47	30	69
Alps	64	Glotzbach, 2013	7.06	45.37	1188	51	6	2	2.29	0.5	1341	385	1280	260	101.73	1.73	109.2	1.85	0	100
Alps	65	Olivetti, 2016	4.68	45.35	1239	55	8	2	1.98	0.33	1087	354	286	24	116.55	2.04	126.5	2.29	91	3
Alps	66	Olivetti, 2016	4.56	45.3	899	146	4	4	3.07	1.75	1766	695	830	260	193.54	1.32	178.1	1.3	61	37
Alps	67	Olivetti, 2016	4.55	45.29	1134	52	7	2	2.11	0.46	1240	421	244	27	128.53	0.88	134.6	0.94	76	24
Alps	69	Olivetti, 2016	4.41	45.24	1471	125	4	2	2.23	0.58	1716	377	330	90	198.41	3.01	240.7	3.74	100	0
Alps	72	Olivetti, 2016	4.38	45.21	890	50	11	1	0.95	0.09	472	174	39	2	61.44	1.79	58.87	1.81	2	98
Alps	75	Olivetti, 2016	4.29	45.14	1081	79	8	1	1.27	0.14	1030	175	44	3	90.52	1.42	95.43	1.43	68	32

Alps	76	Olivetti, 2016	4.6	45.14	1042	74	8	1	1.19	0.13	970	186	46	4	75.92	1.27	78.17	1.32	9	91
Alps	77	Olivetti, 2016	4.3	45.11	871	8	11	0	0.91	0.02	382	42	67	5	52.85	3.53	49.79	3.32	37	63
Alps	78	Olivetti, 2016	4.66	45.07	1079	49	7	0	1.25	0.08	1081	93	34	2	38.78	0.72	40.64	0.73	23	77
Alps	79	Olivetti, 2016	4.78	45.06	996	80	9	1	1.1	0.13	820	230	49	3	69.39	1.1	70.28	1.16	24	76
Alps	80	Olivetti, 2016	4.72	45.06	995	88	8	1	1.12	0.13	957	137	53	4	50.49	0.34	51.54	0.34	28	72
Alps	81	Olivetti, 2016	4.5	45.04	1071	56	8	0	1.22	0.09	1066	103	46	3	44.04	0.41	45.94	0.46	1	99
Alps	82	Olivetti, 2016	4.39	45.02	1052	53	8	1	1.18	0.09	992	141	79	6	62.07	2.98	63.52	3.1	42	58
Alps	85	Olivetti, 2016	4.53	44.99	1005	48	9	1	1.09	0.08	820	143	47	4	57.53	0.82	58.39	0.86	11	89
Alps	86	Delunel, 2010	6.48	44.99	1031	44	8	0	1.14	0.06	1022	75	39	3	33.52	0.82	34.43	0.85	38	54
Alps	88	Olivetti, 2016	4.81	44.9	964	59	10	1	1.01	0.1	671	221	60	6	59.64	0.21	59.53	0.21	32	68
Alps	89	Delunel, 2010	6.45	44.89	977	65	10	1	1.03	0.11	743	224	64	6	55.76	0.27	55.97	0.28	36	62
Alps	90	Delunel, 2010	6.44	44.88	1028	63	8	1	1.13	0.1	940	162	66	6	65.56	0.54	67.28	0.56	33	64
Him	6	Munack, 2014	76.63	34.5	104	16	-3	4	0.15	0.02	4454	592	63	5	259.83	2.97	93.08	1.04	100	0
Him	10	Dortch, 2011	77.35	34.34	121	4	-10	1	0.16	0.02	5251	217	31	4	107.39	3.75	41.85	1.43	100	0
Him	14	Dortch, 2011	77.76	34.28	115	4	-9	2	0.17	0.02	5154	264	51	9	130.36	1.94	49.66	0.72	100	0
Him	15	Dortch, 2011	77.29	34.25	113	7	-6	4	0.14	0.02	4704	532	39	8	246.32	3.03	93.96	1.16	100	0
Him	16	Munack, 2014	77.45	34.22	118	4	-5	3	0.14	0.01	4808	372	22	2	201.48	1.63	77.58	0.62	100	0
Him	17	Munack, 2014	77.39	34.22	112	5	-3	3	0.13	0.01	4500	376	19	2	162.65	1.68	61.42	0.67	100	0
Him	18	Munack, 2014	77.34	34.21	114	7	-4	5	0.14	0.02	4594	574	33	3	236.83	2.12	90.47	0.78	100	0
Him	19	Munack, 2014	77.34	34.2	113	7	-4	5	0.14	0.02	4546	601	31	3	236.19	2.4	90.17	0.91	100	0
Him	21	Dortch, 2011	77.66	34.16	116	5	-7	3	0.16	0.02	4944	424	20	3	219.68	4.76	84.51	1.79	100	0
Him	23	Scherler, 2014	77.96	31.25	1003	142	3	5	1.33	0.09	3722	641	1060	90	257.21	1.46	246.6	1.56	1	99
Him	24	Scherler, 2014	77.85	31.23	1089	143	7	5	1.34	0.09	3301	735	390	30	244.64	0.78	243.3	0.74	2	96
Him	25	Scherler, 2014	77.83	31.22	1180	52	11	3	1.39	0.07	2685	489	290	20	189.06	1.42	201.5	1.36	0	100
Him	26	Scherler, 2014	77.74	31.15	1268	25	14	2	1.48	0.12	2281	304	310	20	121.81	0.8	134.9	0.92	0	100
Him	27	Scherler, 2014	78.4	30.93	1330	171	4	4	1.38	0.1	3535	621	5370	460	261.41	1.75	290.3	1.75	0	100
Him	28	Morell, 2017	79	30.62	1843	102	11	2	1.55	0.14	2720	432	320	40	242.13	2.72	321.7	3.66	0	100
Him	29	Morell, 2015	79.51	30.53	1879	133	11	3	1.63	0.23	2756	485	640	100	320.17	5.65	429.3	7.49	0	100
Him	30	Morell, 2015	79.32	30.38	1551	228	16	2	1.23	0.14	1863	370	340	50	217.01	4.53	272.9	5.1	0	100
Him	43	Kim, 2017	83.88	28.38	797	313	2	8	0.82	0.44	4007	1146	787	7	438.73	3.59	345.1	3.28	0	100
Him	44	Puchol, 2014	84.29	28.38	797	313	2	8	0.82	0.44	4007	1146	585	5	438.73	3.59	345.1	3.28	49	51
Him	47	Puchol, 2014	84.3	28.37	808	166	6	3	0.56	0.08	3676	558	1700	400	340.32	7.45	289.9	6.22	50	50
Him	49	Kim, 2017	83.88	28.36	808	166	6	3	0.56	0.08	3676	558	2600	200	340.32	7.45	289.9	6.22	0	100
Him	50	Kim, 2017	83.96	28.34	808	166	6	3	0.56	0.08	3676	558	900	100	340.32	7.45	289.9	6.22	0	100
Him	51	Kim, 2017	83.89	28.34	808	166	6	3	0.56	0.08	3676	558	900	100	340.32	7.45	289.9	6.22	0	100
Him	52	Puchol, 2014	84.33	28.33	830	331	3	8	0.85	0.49	3909	1165	340	2	425.18	3.2	336.2	3.06	53	47
Him	56	Godard, 2012	84.41	28.32	858	187	7	4	0.6	0.13	3526	608	3300	600	338.45	6.39	292.3	5.22	1	99
Him	58	Godard, 2014	83.77	28.31	858	187	7	4	0.6	0.13	3526	608	2900	300	338.45	6.39	292.3	5.22	0	100
Him	65	Godard, 2012	84.36	28.28	1000	214	10	4	0.91	0.5	2979	774	2000	400	387.52	3.03	356	3.34	37	63
Him	68	Godard, 2014	83.74	28.28	1000	214	10	4	0.91	0.5	2979	774	800	100	387.52	3.03	356	3.34	0	100
Him	73	Andermann, 2011	85.37	28.23	543	216	-2	8	0.75	0.32	4677	1074	2500	300	406.09	1.28	282.2	0.95	0	100

Him	74	Andermann, 2011	85.3	28.18	834	294	6	8	0.86	0.48	3453	1205	2800	300	409.37	2.15	328.9	1.98	0	100
Him	76	Wobus, 2005	84.85	28.14	1483	239	13	2	1.49	0.82	2389	549	630	90	256.86	3.18	291.9	3.77	0	100
Him	78	Andermann, 2011	85.31	28.11	1013	468	6	9	1.11	0.73	3454	1335	585	3	370.32	3.22	314.7	2.2	0	100
Him	80	Andermann, 2011	84.83	28.1	1553	448	14	4	1.77	0.88	2205	846	410	2	204.79	5.8	230.5	5.01	0	100
Him	81	Wobus, 2005	84.83	28.1	1042	495	6	9	1.14	0.75	3394	1357	559	4	356.33	3.22	305.1	2.22	0	100
Him	83	Portenga, 2015	89.71	28.06	574	258	-1	8	0.77	0.35	4558	1162	2600	300	404.72	1.17	283.5	0.88	0	97
Him	90	Godard, 2014	85.18	27.98	1291	603	9	9	1.41	0.85	2885	1385	669	2	295.6	3.68	279.1	2.26	0	100
Him	92	Andermann, 2011	85.19	27.98	1935	194	17	1	2.38	0.62	1525	328	780	150	106.9	3.9	139.7	4.93	0	90
Him	93	Godard, 2014	85.19	27.98	808	252	7	4	0.78	0.21	3518	736	1360	170	430.89	8.72	351.1	8.17	0	90
Him	95	Wobus, 2005	84.73	27.95	1045	222	10	3	0.92	0.24	2973	538	2030	180	238.65	1.7	229.7	1.54	0	100
Him	96	Andermann, 2011	85.13	27.93	1105	531	9	9	1.24	0.61	2894	1539	1200	100	371.51	3.88	319.7	1.94	0	100
Him	97	Wobus, 2005	84.73	27.93	1261	107	15	2	1.4	0.25	2019	525	370	40	283.8	9.07	313	9.92	0	100
Him	98	Godard, 2014	85.14	27.92	2367	249	20	1	1.96	0.06	946	240	300	100	58.64	1.7	85.5	2.28	0	100
Him	101	Roux-Mallouf, 2015	89.74	27.89	1486	227	17	2	1.59	0.07	1429	423	730	50	173.14	2.35	200.2	2.52	0	100
Him	104	Wobus, 2005	84.74	27.88	298	37	-1	3	0.42	0.03	4572	472	335	28	177.57	1.93	100.2	1.08	0	100
Him	105	Godard, 2014	84.63	27.87	297	33	-1	3	0.43	0.04	4652	477	1174	99	182.6	2.57	103.2	1.48	0	100
Him	107	Portenga, 2015	89.87	27.86	299	39	-5	4	0.44	0.06	4978	509	1816	159	220.19	2.67	123.5	1.58	0	100
Him	110	Godard, 2014	84.97	27.81	868	620	3	11	0.99	0.54	3799	1690	2000	300	346.53	0.91	261.6	0.57	0	100
Him	111	Godard, 2014	84.89	27.81	1491	166	15	3	1.38	0.21	1908	647	1330	220	216.41	2.93	252.5	2.93	36	64
Him	113	Olen, 2015	87.37	27.77	1448	286	14	4	1.3	0.26	2140	855	880	50	231.3	2.67	259.6	2.26	0	100
Him	114	Godard, 2014	85.86	27.75	1452	283	14	4	1.3	0.25	2131	850	850	160	231.95	2.72	260.5	2.3	0	100
Him	115	Godard, 2014	85.07	27.75	307	46	-4	4	0.44	0.06	4933	544	1383	119	216.74	2.25	122.4	1.34	21	79
Him	116	Olen, 2015	87.35	27.74	2105	86	21	1	1.55	0.07	792	164	190	30	64.9	0.79	90.11	1.1	0	100
Him	117	Adams, 2016	91.15	27.72	1698	109	18	2	1.4	0.14	1242	359	460	30	121.58	2.18	152.3	2.61	0	100
Him	119	Adams, 2016	91.15	27.72	1703	115	18	2	1.4	0.14	1234	363	520	100	118.98	2.04	149.2	2.45	0	100
Him	121	Adams, 2016	91.17	27.69	942	684	4	11	1.02	0.55	3640	1783	1900	300	322.91	0.9	250.9	0.52	0	100
Him	126	Godard, 2014	85.73	27.68	2027	92	20	1	1.48	0.08	896	241	180	20	89.36	1.6	121.5	2.23	0	100
Him	127	Adams, 2016	89.77	27.67	2037	95	20	1	1.48	0.07	917	249	490	70	137.31	1.33	187.6	1.85	0	98
Him	128	Portenga, 2015	89.77	27.67	344	21	-2	1	0.45	0.01	4707	183	198	17	112.88	3.28	68.76	2.02	0	98
Him	129	Adams, 2016	91.44	27.66	357	25	-1	1	0.46	0.01	4613	215	1148	95	123.1	3.31	75.93	2.11	0	100
Him	130	Olen, 2015	87.36	27.66	349	31	-2	2	0.46	0.01	4707	266	693	58	168.46	2.46	102.6	1.49	0	100
Him	131	Roux-Mallouf, 2015	89.87	27.66	1983	72	18	3	1.52	0.25	1241	469	200	20	119.85	2.41	163.5	3.34	0	100
Him	133	Roux-Mallouf, 2015	89.8	27.63	1983	74	20	2	1.4	0.15	947	327	210	30	92.4	3.04	125.4	4.16	0	100
Him	135	Adams, 2016	91.49	27.62	1849	416	9	2	1.76	0.39	3067	422	470	40	280.14	3.53	345.7	3.15	0	100
Him	136	Andermann, 2011	86.09	27.62	2031	63	16	2	1.9	0.11	1710	405	710	120	170.2	1.01	233.1	1.41	0	100
Him	137	Adams, 2016	90.67	27.61	1941	119	17	2	1.54	0.32	1479	401	190	20	136.52	1.51	186.1	2.09	0	95
Him	140	Olen, 2015	87.28	27.59	620	167	7	4	0.81	0.35	3421	736	250	30	369.17	5.33	269.7	4.48	0	100
Him	142	Roux-Mallouf, 2015	89.85	27.59	777	611	-3	9	0.96	0.5	4748	1176	1480	110	416.46	3.28	272.3	2.73	0	100
Him	143	Adams, 2016	91.49	27.58	1049	131	14	2	1.35	0.22	2193	401	131	11	208.25	3.37	215.5	3.54	0	100
Him	144	Roux-Mallouf, 2015	89.63	27.58	704	185	8	4	0.91	0.41	3225	733	340	40	355.78	4.89	282.2	3.8	0	100
Him	146	Adams, 2016	90.44	27.56	481	189	2	5	0.6	0.28	4154	772	575	47	371.94	3.83	239.6	2.82	0	100

Him	147	Olen, 2015	87.31	27.56	443	188	-1	6	0.56	0.24	4442	873	1124	93	348.22	1.23	214.5	0.87	0	100
Him	148	Adams, 2016	91.52	27.55	1889	139	17	1	1.65	0.22	1513	317	120	10	168.67	1.97	227.5	2.58	0	99
Him	149	Roux-Mallouf, 2015	89.66	27.54	766	156	10	4	1.09	0.39	2903	650	1130	137	273.95	1.72	231.8	1.06	0	100
Him	151	Adams, 2016	90.44	27.54	917	153	10	3	0.87	0.2	3031	498	306	25	235.58	1.33	218.1	1.24	0	100
Him	152	Roux-Mallouf, 2015	89.8	27.53	2402	130	14	2	2.27	0.1	2183	468	2300	210	267.49	4.06	391.6	6.42	0	100
Him	153	Adams, 2016	89.87	27.53	920	149	14	2	1.44	0.32	2337	416	210	30	230.92	2.96	216.4	2.89	0	100
Him	154	Portenga, 2015	89.87	27.52	1610	165	19	1	1.2	0.23	1229	241	120	10	66.66	1.85	83.54	2.53	0	100
Him	156	Adams, 2016	91.17	27.52	854	670	1	9	0.96	0.53	4248	1344	2160	220	387.35	1.17	271.8	0.89	0	92
Him	158	Olen, 2015	87.19	27.51	1965	68	16	2	1.72	0.17	1776	381	270	10	163.96	1.98	223	2.66	0	100
Him	159	Adams, 2016	90.66	27.51	808	110	6	2	0.75	0.13	3572	376	80	10	154.77	1.6	134.9	1.27	0	100
Him	160	Portenga, 2015	89.79	27.51	419	220	-1	6	0.62	0.22	4551	842	1880	310	381.94	1.96	226.6	1.39	0	100
Him	162	Adams, 2016	90.66	27.5	2158	429	12	4	2.06	0.4	2559	680	####	760	303.05	3.51	401.9	4.36	0	100
Him	163	Roux-Mallouf, 2015	89.44	27.5	500	257	1	7	0.66	0.4	4224	1064	996	85	333.15	0.98	209.7	0.71	0	100
Him	164	Adams, 2016	90.67	27.5	1085	202	16	1	1.79	0.26	2008	325	90	9	173.1	1.49	171.6	1.36	0	100
Him	165	Adams, 2016	90.67	27.5	999	154	10	3	0.95	0.22	2919	503	179	15	208.2	0.69	199.7	0.67	0	100
Him	166	Adams, 2016	90.52	27.49	698	122	6	3	0.77	0.14	3549	455	170	20	225.91	1.62	182.8	1.2	0	100
Him	167	Olen, 2015	87.16	27.48	1150	752	2	9	1.23	0.63	4011	1250	940	70	399.39	4.2	313.4	4.79	0	100
Him	169	Adams, 2016	90.35	27.47	2106	362	13	4	2.03	0.33	2429	726	530	40	292.21	2.91	391.5	3.04	0	100
Him	170	Adams, 2016	89.9	27.46	1081	129	12	2	1.02	0.19	2702	411	166	13	237.18	4.22	240.3	4.64	0	94
Him	171	Portenga, 2015	89.9	27.46	876	68	8	1	0.93	0.13	3165	285	50	5	159.67	2.36	148.8	2.09	0	94
Him	172	Roux-Mallouf, 2015	89.44	27.45	1428	698	6	6	1.41	0.61	3467	1022	1360	100	425.78	3.27	418	4.57	0	100
Him	173	Adams, 2016	90.96	27.44	1133	39	11	2	1.21	0.19	2724	319	98	8	175.4	2.18	184.6	2.4	0	100
Him	174	Adams, 2016	89.68	27.43	962	60	12	3	1.36	0.29	2562	391	120	13	169.86	1.59	166.9	1.56	0	100
Him	175	Adams, 2016	89.68	27.43	1036	142	14	3	1.52	0.37	2380	462	134	13	197.03	1.27	196.6	1.34	0	100
Him	177	Adams, 2016	91.55	27.4	979	627	5	8	1.08	0.52	3648	1185	4310	790	397.18	1.82	311.7	1.72	0	100
Him	178	Olen, 2015	87.15	27.39	985	138	12	4	1.17	0.34	2663	633	252	21	264.24	1.15	257	1.32	0	100
Him	179	Adams, 2016	90.54	27.37	568	477	0	8	0.75	0.41	4426	1114	5240	1060	413.69	1.17	252.1	0.87	0	100
Him	181	Adams, 2016	91.67	27.36	918	73	7	2	0.83	0.1	3400	268	48	4	102.99	1.99	97.73	1.76	0	98
Him	182	Adams, 2016	91.62	27.34	1041	54	12	2	1.24	0.23	2754	332	146	11	166.25	4.61	170.2	4.72	0	92
Him	184	Adams, 2016	89.48	27.33	909	100	7	2	0.81	0.11	3475	288	79	7	105.82	0.94	98.03	0.76	0	100
Him	186	Adams, 2016	89.97	27.3	963	75	7	2	0.86	0.11	3441	302	117	14	110.92	1.59	107.1	1.47	0	100
Him	188	Adams, 2016	90.01	27.29	1037	85	9	2	1.03	0.2	3059	379	208	19	221.64	3.18	220.2	3.3	98	2
Him	189	Portenga, 2015	90.04	27.27	2310	162	17	2	2.01	0.42	1518	440	1000	60	256.79	8.33	377.3	12.3	1	90
Him	190	Adams, 2016	90.02	27.27	1870	564	14	3	1.83	0.42	2143	628	5270	1050	329.26	7.79	386.6	9.11	0	91
Him	191	Adams, 2016	90.05	27.26	1131	87	9	1	1.02	0.12	3060	226	102	10	139.86	2.4	145.6	2.6	83	17
Him	192	Portenga, 2015	90.05	27.26	1124	110	13	3	1.52	0.41	2460	527	132	12	215.71	1.24	225.1	1.28	83	17
Him	193	Roux-Mallouf, 2015	89.53	27.23	1124	109	13	3	1.52	0.41	2462	530	368	32	214.63	1.24	224	1.28	0	95
Him	194	Roux-Mallouf, 2015	89.48	27.23	925	79	10	2	0.99	0.15	3092	290	50	5	156.4	4.14	148.5	3.95	0	91
Him	195	Olen, 2015	87.24	27.21	843	38	5	1	0.71	0.03	3770	119	42	4	44.82	0.56	41.03	0.52	0	100
Him	197	Olen, 2015	87.26	27.18	1066	109	8	2	0.99	0.15	3198	314	65	6	166.5	2.02	167.7	2.05	0	100
Him	200	Olen, 2015	87.25	27.12	1856	201	21	1	1.15	0.32	871	276	220	10	131.34	2.09	177.1	3.2	0	100

Him	203	Roux-Mallouf, 2015	89.59	26.95	1272	173	12	3	1.18	0.28	2592	629	1541	156	294.96	3.09	317.9	3.43	0	100
Him	204	Roux-Mallouf, 2015	89.59	26.94	1294	176	13	3	1.24	0.31	2504	670	574	55	297.74	1.55	329.9	2.02	0	100
Him	206	Roux-Mallouf, 2015	89.6	26.88	1160	175	8	2	1.09	0.22	3118	388	45	4	194.76	1.65	200.5	2.11	0	100
Jap	1	Byun, 2015	128.71	37.74	1386	12	7	0	2.11	0.05	1083	86	72	13	31.15	1.09	36.15	1.28	100	0
Jap	2	Byun, 2015	128.72	37.72	1381	11	7	0	2.09	0.05	1033	90	102	23	38.73	0.65	44.87	0.75	100	0
Jap	8	Regalla, 2013	140.92	37.41	1316	15	11	0	1.67	0.06	486	105	130	4	76.28	1.71	86.56	1.93	100	0
Jap	10	Regalla, 2013	140.95	37.31	1327	20	11	0	1.68	0.07	451	126	186	6	64.87	0.82	73.92	0.93	85	7
Jap	12	Korup, 2014	137.76	35.72	2094	125	2	2	3.7	0.69	2114	337	1770	450	171.4	1.76	241.6	2.4	98	2
Ken	1	Acosta, 2015	36.84	1.91	459	8	21	0	0.29	0.01	1411	41	5	0	14.93	0.25	10.55	0.18	0	100
Ken	5	Roller, 2012	30.05	0.66	1522	32	16	2	1.12	0.13	2290	460	70	3	284.7	8.12	343.6	9.8	0	100
Ken	6	Roller, 2012	30.17	0.66	1473	9	16	1	1.07	0.07	2216	236	56	2	106.43	3.26	126.6	3.86	0	100
Ken	7	Roller, 2012	29.98	0.64	1532	76	15	4	1.21	0.27	2441	700	47	2	232.29	1.95	283.7	2.42	0	96
Ken	9	Roller, 2012	30.15	0.59	1496	39	15	2	1.13	0.12	2385	319	46	2	149.98	1.29	180.7	1.62	0	100
Ken	13	Roller, 2012	30.01	0.21	1667	187	11	4	1.48	0.47	2970	737	131	15	293.7	3.63	380.4	4.89	0	100
Ken	14	Roller, 2012	29.95	0.12	1653	181	12	5	1.47	0.53	2924	797	113	3	268.42	2.81	346.3	3.91	0	98
Ken	16	Roller, 2012	29.75	0.08	1420	98	16	3	1	0.19	2105	485	37	1	155.08	2.85	184.6	3.69	0	95
Saf	1	Chadwick, 2013	31.28	-23.04	564	56	23	0	0.32	0.04	413	52	7	1	12.09	0.04	9.59	0.03	1	98
Saf	2	Chadwick, 2013	31.24	-23.04	492	7	23	0	0.27	0.01	344	14	5	1	6.16	0.1	4.49	0.07	15	85
Saf	3	Chadwick, 2013	31.29	-23.12	548	39	23	0	0.31	0.03	404	44	5	1	10.97	0.06	8.55	0.04	11	89
Saf	4	Glotzbach, 2016	31.49	-23.93	536	6	22	0	0.32	0	365	17	7	1	8.19	0.09	6.2	0.06	21	79
Saf	5	Glotzbach, 2016	31.24	-23.94	542	5	22	0	0.32	0	404	11	3	0	7.02	0.11	5.34	0.08	0	100
Saf	6	Glotzbach, 2016	31.67	-24.73	635	8	22	0	0.41	0.01	377	17	4	0	7.73	0.09	6.31	0.08	100	0
Saf	7	Chadwick, 2013	31.5	-25.03	656	23	21	0	0.43	0.01	431	58	6	1	14.63	0.11	12.24	0.09	100	0
Saf	8	Glotzbach, 2016	31.26	-25.1	715	16	21	0	0.46	0.02	568	44	5	1	16.74	0.12	14.46	0.11	100	0
Saf	9	Glotzbach, 2016	31.22	-25.12	715	16	21	0	0.46	0.02	568	44	5	1	16.74	0.12	14.46	0.11	100	0
Saf	10	Glotzbach, 2016	31.71	-25.19	730	13	21	0	0.48	0.01	595	34	3	0	15.95	0.11	13.88	0.1	100	0
Saf	11	Chadwick, 2013	31.27	-25.22	629	4	22	0	0.43	0	332	17	4	0	8.76	0.12	7.11	0.11	100	0
Saf	12	Chadwick, 2013	31.27	-25.24	709	17	21	0	0.47	0.01	579	35	4	0	15.11	0.13	13.03	0.11	100	0
Saf	13	Glotzbach, 2016	31.43	-25.31	708	16	21	0	0.48	0.02	576	35	5	1	14.97	0.11	12.89	0.09	100	0
Saf	14	Glotzbach, 2016	31.39	-25.33	683	16	21	0	0.47	0.01	501	50	10	1	19.49	0.19	16.51	0.16	100	0
Mad	1	Cox, 2009	48.2	-17.63	1198	9	21	0	0.68	0	825	29	20	3	5.94	0.15	6.44	0.16	34	66
Nam	1	Bierman, 2007	17.26	-21.84	418	13	19	0	0.25	0.01	1616	68	6	1	13.99	0.11	9.53	0.07	0	100
Bra	2	Barreto, 2013	-43.45	-19.23	1563	37	19	1	1.08	0.03	1073	166	4	0	90.47	2.2	111.3	2.75	0	98
Bra	7	Salgado, 2007	-43.66	-20.37	1506	19	18	0	1.12	0.03	1213	81	4	2	35.43	0.95	42.75	1.15	29	68
Bra	16	Salgado, 2016	-44.63	-22.25	1890	98	14	1	1.51	0.11	1747	165	16	1	86.82	2.46	117.2	3.46	97	3
Bra	17	Rezende, 2013	-44.63	-22.25	1893	97	14	1	1.52	0.11	1750	163	15	0	87.86	2.82	118.7	3.97	97	3
Bra	18	Salgado, 2016	-44.64	-22.25	1979	124	14	1	1.6	0.13	1848	180	11	0	89.49	1.99	123.4	2.68	83	17
Bra	19	Salgado, 2016	-44.5	-22.25	1719	96	16	1	1.32	0.11	1462	195	15	1	81.35	2.12	105	2.71	29	71
Bra	20	Rezende, 2013	-44.5	-22.25	1717	94	16	1	1.31	0.11	1458	193	12	1	80.53	2.24	103.8	2.85	28	72
Bra	22	Salgado, 2016	-44.64	-22.27	2033	92	13	1	1.65	0.1	1916	135	12	0	64.53	1.34	89.62	1.85	95	5
Bra	23	Rezende, 2013	-44.64	-22.27	2035	92	13	1	1.66	0.1	1921	136	14	1	64.65	1.45	89.85	2.01	94	6

Bra	24	Salgado, 2016	-44.54	-22.28	1853	129	15	1	1.45	0.15	1642	232	19	1	123.05	1.69	165.1	2.24	0	100
Bra	25	Rezende, 2013	-44.54	-22.28	1845	128	15	1	1.44	0.15	1632	230	18	1	117.93	1.58	157.8	2.17	0	100
Bra	29	Salgado, 2016	-44.59	-22.32	1879	152	15	1	1.48	0.17	1686	252	20	1	112.82	2.74	152.2	3.75	41	59
Bra	30	Gonzalez, 2016	-43	-22.49	1784	64	15	2	1.5	0.17	1383	512	46	3	207.04	4.44	269.9	5.91	100	0
Bra	31	Salgado, 2016	-44.59	-22.67	1626	114	17	2	1.19	0.15	1121	315	22	1	120.63	4.11	152	5.45	25	75
Bra	32	Salgado, 2016	-44.53	-22.67	1626	100	17	1	1.2	0.13	1163	257	23	1	121.71	1.23	153.7	1.52	7	93
Bra	33	Salgado, 2016	-44.68	-22.69	1619	104	17	2	1.19	0.15	1131	319	27	2	112.22	3.52	140.6	4.57	1	99
Bra	39	Salgado, 2016	-44.55	-22.96	1683	101	19	2	1.08	0.08	710	370	49	9	140.2	3.13	174.9	3.84	15	85
Bra	43	Salgado, 2014	-48.75	-25.32	1916	50	18	2	1.53	0.07	745	445	20	1	123.84	2.83	166.2	3.77	92	6
SInd	23	Mandal, 2015	75.58	12.48	3316	270	21	0	2.24	0.24	1090	104	30	3	21.16	0.83	37.16	1.42	0	100
SInd	25	Mandal, 2015	75.71	12.45	3424	247	21	0	2.32	0.21	1073	78	30	3	24.08	1.07	42.77	1.83	0	100
SInd	27	Mandal, 2015	75.42	12.45	3224	926	22	1	2.15	0.87	955	106	24	2	10.31	0.11	18.45	0.2	100	0
SInd	35	Mandal, 2015	75.75	12.09	795	31	25	1	0.5	0.03	739	208	41	4	46.54	0.18	41.61	0.16	100	0
SInd	44	Mandal, 2015	75.75	11.77	3178	506	22	1	2.31	0.41	831	146	21	2	9.51	0.14	16.37	0.24	100	0
SInd	45	Mandal, 2015	75.81	11.7	3725	86	23	0	2.87	0.1	826	73	15	2	14.34	0.53	26.07	0.96	78	22
SInd	46	Mandal, 2015	75.8	11.69	4085	126	24	1	2.77	0.19	548	231	40	3	87.39	1.22	163.5	2.34	88	12
SInd	52	Mandal, 2015	76.01	11.41	1802	339	18	3	1.47	0.3	1530	581	22	2	94.95	2.28	123.2	2.6	46	54
SInd	62	Mandal, 2015	76.36	11.15	1515	147	15	1	1.59	0.13	2092	149	10	1	76.01	1.19	90.11	1.42	46	54
SInd	68	Mandal, 2015	76.57	10.92	980	659	25	3	0.61	0.48	678	356	23	2	39.85	0.05	38.98	0.05	4	96
SInd	79	Blanckenburg, 2004	80.66	7.15	2651	455	20	3	1.92	0.19	1221	448	17	2	84.53	0.56	126.1	0.75	0	94
SInd	80	Blanckenburg, 2004	80.75	7.13	2490	399	22	3	1.79	0.24	1014	460	45	5	67.05	0.42	100.6	0.59	0	96
SInd	84	Vanacker, 2007	80.78	6.72	2531	81	22	1	1.82	0.04	929	187	22	2	60.13	1.71	90.68	2.55	0	100
Taw	3	Derrieux, 2014	121.46	23.97	3147	790	13	4	3.27	1.26	1871	710	6500	1900	246.79	1.88	432.7	3.57	0	100
Taw	4	Derrieux, 2014	121.12	23.14	3124	815	13	4	3.18	1.27	1832	650	3300	1100	212.15	1.94	376.5	3.52	0	100

Table DR2

TABLE DR2. E-K_{SN} POWER LAW CONSTANTS AND GOODNESS OF FIT METRICS

	Morphological steady-state threshold R^2 = 0.75					Morphological steady-state threshold R^2 = 0.8				
MAP (mm/y	p	C	*R^2	†χ^2	KS p-value§	p	C	*R^2	†χ^2	KS p-value§
297-705	1.96	1.67E-08	0.5	4580	0.33	1.94	1.82E-08	0.49	4343	0.38
705-908	2.16	4.01E-09	0.26	6578	0.72	2.1	6.20E-09	0.23	6358	0.52
908-1123	1.80	2.45E-08	0.4	4986	0.33	1.93	1.17E-08	0.35	4585	0.19
1123-1386	1.80	4.38E-08	0.24	5522	0.44	1.77	5.64E-08	0.27	4721	0.82
1386-1717	3.30	1.56E-11	0.31	3750	0.33	3.71	2.01E-12	0.29	3503	0.52
1717-4085	3.18	5.88E-11	0.54	2680	**0.01**	3.16	6.42E-11	0.55	2383	**0.05**
MAT (°C)										
-5-3	3.21	1.67E-11	0.21	5861	**0.04**	3.7	1.03E-12	0.2	5361	**0.01**
3-7	2.48	1.12E-09	0.5	4320	0.23	2.32	2.69E-09	0.49	4012	0.27
7-10	2.16	4.42E-09	0.57	3344	0.43	2.37	1.69E-09	0.49	3809	0.53
10-13	2.13	6.08E-09	**-0.36**	9984	0.11	2.11	6.74E-09	**-0.47**	9310	0.12
13-16	3.69	1.50E-12	0.26	3513	**0.02**	3.83	8.20E-13	0.39	2766	**0.05**
16-25	1.66	6.73E-08	**0.09**	2602	**0.08**	1.62	7.10E-08	**-0.08**	3099	**0.08**
AI										
0.25-0.65	1.97	1.92E-08	0.72	2405	0.44	1.95	2.17E-08	0.71	2342	0.52
0.65-1	1.80	2.89E-08	0.19	8750	0.16	1.85	2.24E-08	0.18	7863	0.08
1-1.2	2.17	2.74E-09	0.43	4152	0.23	2.13	3.58E-09	0.42	3956	0.27
1.2-15.	2.50	7.32E-10	0.44	4110	0.44	2.65	3.01E-10	0.43	3624	0.52
1.5-1.9	3.14	4.08E-11	0.42	3173	0.33	2.96	1.07E-10	0.45	2946	0.38
1.9-3.8	1.86	4.45E-08	**-0.3**	9014	0.75	1.95	2.91E-08	**-0.22**	7471	0.82
ME (m)										
332-826	1.47	1.19E-07	**-0.06**	2575	0.95	1.45	1.21E-07	**-0.12**	2809	0.99
826-1239	2.67	1.27E-09	**0.03**	2885	**0.04**	2.28	6.43E-09	**0.01**	2462	0.11
1239-1771	3.53	9.36E-12	0.31	2343	**0.01**	3.86	1.94E-12	0.38	1962	**0.02**
1771-2361	4.06	2.83E-13	0.38	3077	0.72	4.15	1.73E-13	0.30	3203	0.82
2361-3197	4.21	3.57E-14	0.38	3535	0.44	4.35	1.62E-14	0.34	3411	0.52
3197-4977	4.10	7.37E-14	0.24	5921	**0.01**	3.69	8.21E-13	0.17	5641	**0.02**

*R^2 statistical goodness of fit

†χ^2 statistical goodness of fit

§Two sample Kolmogorov-Smirnov two sided p-value test at 90% significance level. H_0 = Calculated and modeled k_{sn} are from same continuous distribution.

TABLE DR2. E-K_{SN} POWER LAW CONSTANTS AND GOODNESS OF FIT METRICS (CONTINUED)

	Morphological steady-state threshold R^2 = 0.85					Morphological steady-state threshold R^2 = 0.9				
MAP (mm/y	p	C	*R^2	†χ^2	KS p-value§	p	C	*R^2	†χ^2	KS p-value§
297-705	1.87	2.68E-08	0.53	3191	0.38	1.78	4.28E-08	0.50	2797	0.56
705-908	2.08	7.45E-09	0.28	4891	0.7	1.99	1.24E-08	0.48	2981	0.75
908-1123	1.76	2.73E-08	**0.01**	5407	0.16	2.01	7.98E-09	0.38	2860	0.26
1123-1386	1.98	1.53E-08	0.15	4437	0.55	2.20	5.54E-09	0.28	2806	0.91
1386-1717	3.24	2.36E-11	0.33	3123	0.26	3.02	6.64E-11	0.32	2502	0.16
1717-4085	3.08	8.44E-11	0.48	2473	**0.03**	3.27	3.06E-11	0.51	1982	**0.08**
MAT (°C)										
-5-3	4.3	3.60E-14	0.14	4516	**0.01**	2.97	6.37E-11	0.18	3734	**0.05**
3-7	2.23	4.34E-09	0.51	3260	0.38	2.30	3.24E-09	0.53	2514	0.75
7-10	2.45	1.02E-09	0.61	2326	0.38	2.40	1.05E-09	0.70	1350	0.91
10-13	2.08	7.65E-09	**-0.61**	8323	0.26	2.40	1.70E-09	**-0.24**	4762	0.26
13-16	4.98	2.07E-15	0.41	2131	0.11	4.14	1.52E-13	0.43	1783	0.56
16-25	1.76	4.91E-08	0.3	2117	0.14	1.75	5.20E-08	0.52	1256	0.32
AI										
0.25-0.65	1.92	2.62E-08	0.71	1990	0.7	1.84	3.90E-08	0.77	1246	0.91
0.65-1	1.97	1.22E-08	0.35	4794	0.38	2.01	1.01E-08	0.40	3561	0.75
1-1.2	2.12	3.74E-09	0.33	3524	0.26	2.24	2.17E-09	0.49	2233	0.26
1.2-15.	2.72	2.32E-10	0.4	3128	0.7	2.90	7.94E-11	0.41	2455	0.91
1.5-1.9	3.28	1.38E-11	0.51	2103	0.38	3.60	2.43E-12	0.54	1491	0.56
1.9-3.8	1.69	1.21E-07	**-0.35**	7788	0.76	1.73	1.09E-07	**-0.13**	5313	0.81
ME (m)										
332-826	1.26	2.52E-07	**-0.3**	2387	0.53	1.35	1.71E-07	**-0.28**	1781	0.56
826-1239	3.38	6.85E-11	0.06	1862	**0.04**	2.60	1.70E-09	0.19	1310	0.16
1239-1771	3.78	2.41E-12	0.37	1898	**0.04**	3.95	1.04E-12	0.35	1321	**0.09**
1771-2361	6.09	5.33E-18	0.2	2506	0.53	5.29	4.28E-16	0.30	2028	0.91
2361-3197	4.5	6.51E-15	0.44	2228	0.7	4.65	3.22E-15	0.45	1766	0.91
3197-4977	3.41	4.02E-12	0.19	4921	**0.03**	3.26	9.00E-12	0.27	3850	**0.04**

*R^2 statistical goodness of fit

†χ^2 statistical goodness of fit

§Two sample Kolmogorov-Smirnov two sided p-value test at 90% significance level. H_0 = Calculated and modeled k_{sn} are from same continuous distribution.

TABLE DR2. E-K_{SN} POWER LAW CONSTANTS AND GOODNESS OF FIT METRICS (CONTINUED)

	Morphological steady-state threshold R^2 = 0.9 (fixed p)					Morphological steady-state threshold R^2 = 0.95				
MAP (mm/y	p	C_{ne}	*R^2	†χ^2	KS p-value§	p	C	*R^2	†χ^2	KS p-value§
297-705	2.18	7.28E-09	0.68	1807	0.16	1.64	9.66E-08	0.55	1233	0.88
705-908	2.18	4.75E-09	0.54	2646	0.26	2.01	1.12E-08	0.52	1704	0.88
908-1123	2.18	3.37E-09	0.55	2093	0.26	2.82	9.46E-11	0.54	1107	0.24
1123-1386	2.18	6.09E-09	0.26	2865	0.91	1.8	2.89E-08	0.66	928	0.99
1386-1717	2.18	3.38E-09	**0.09**	3377	0.16	5.48	1.79E-16	0.39	857	0.41
1717-4085	2.18	4.65E-09	**-1.20**	8855	**0.01**	2.94	1.81E-10	0.56	1128	0.3
MAT (°C)										
-5-3	2.18	4.81E-09	**0.02**	4480	0.39	2.6	4.50E-10	0.29	2158	0.41
3-7	2.18	5.67E-09	0.48	2753	0.75	2.49	6.40E-10	0.64	1031	0.88
7-10	2.18	3.04E-09	0.68	1448	0.91	3.21	2.41E-11	0.58	1020	0.88
10-13	2.18	4.79E-09	**-0.76**	6764	0.26	3.22	2.51E-11	0.28	1545	0.12
13-16	2.18	2.30E-09	**-2.59**	11139	0.16	6.74	2.22E-19	0.35	916	0.41
16-25	2.18	1.10E-08	0.62	1006	0.13	1.61	9.13E-08	0.4	724	0.49
AI										
0.25-0.65	2.18	9.69E-09	0.77	1209	0.16	1.81	5.61E-08	0.7	727	0.65
0.65-1	2.18	4.18E-09	0.49	3017	0.75	1.89	1.90E-08	0.33	2206	0.88
1-1.2	2.18	2.80E-09	0.43	2470	0.26	2.88	7.48E-11	0.81	560	0.88
1.2-15.	2.18	2.79E-09	**-0.14**	4743	0.75	3.15	1.91E-11	0.51	1134	0.88
1.5-1.9	2.18	2.34E-09	**-0.44**	4716	0.39	4.84	7.12E-15	0.29	1128	0.41
1.9-3.8	2.18	1.33E-08	0.37	2951	0.21	2.48	1.64E-09	0.16	2239	0.92
ME (m)										
332-826	2.18	9.70E-09	0.26	1031	**0.09**	1.34	1.62E-07	**-0.26**	1088	0.65
826-1239	2.18	8.89E-09	0.12	1411	0.16	2.2	7.54E-09	0.25	717	0.24
1239-1771	2.18	3.86E-09	**-1.24**	4576	**0.05**	5.85	6.57E-17	0.44	681	0.88
1771-2361	2.18	4.56E-09	**-2.20**	9284	**0.05**	4.12	2.04E-13	0.29	1267	0.65
2361-3197	2.18	2.03E-09	**-3.76**	15250	**0.09**	5.22	1.65E-16	0.46	939	0.65
3197-4977	2.18	3.72E-09	**-0.33**	7035	0.21	2.94	4.96E-11	0.39	2044	0.3

*R^2 statistical goodness of fit

†χ^2 statistical goodness of fit

§Two sample Kolmogorov-Smirnov two sided p-value test at 90% significance level. H_0 = Calculated and modeled k_{sn} are from same continuous distribution.